Structural and AMS analyses of basement granitoid rocks of the Chitrial area and its bearing on Unconformity proximal type uranium mineralization, Cuddapah basin, Telangana

Synopsis (in 5000 words) of the research work under the Ph.D. programme in the department of Geology of Presidency University, Kolkata

SUBMITTED BY

PARAMITA DAS

REGISTRATION No. – 14RS15210003

PRESIDENCY UNIVERSITY
KOLKATA

2018

Supervisor

Dr. Gautam Ghosh

Department of Geology,

Presidency University,

Kolkata 700073

Structural and AMS analyses of basement granitoid rocks of the Chitrial area and its bearing on Unconformity proximal type uranium mineralization, Cuddapah basin, Telangana

1. INTRODUCTION

Studies in many of the well-known unconformity-proximal type uranium deposits of the world have established that structure of the basement rocks played an important role in emplacement and genesis of uranium mineralization (Jefferson et al., 2007). Most unconformity associated uranium deposits occur within and along major tectonic discontinuities that developed in the basement during major orogenies (Jefferson et al., 2007). Mercadier et al. (2010) described that in P-Patch uranium deposit of Athabasca Basin, Canada; dense networks of micro-fractures within basement rocks favoured the percolation of basinal fluids down to considerable depths, thereby facilitating uranium mobility within the basement rocks and the formation of unconformity type mineralization. Though in India unconformity associated uranium deposits are known over a couple of decades, detailed structural analyses of such deposits are lacking till date. Detailed analyses of mesoscopic and microscopic structures of the host rock for mineralization are essential for reconstruction of deformational sequence and its correlation with grain scale deformation processes to understand the structural control, deformation tectonics and syn to post kinematic remobilization of such deposits. A Mesoproterozoic unconformity associated uranium deposits occur at Chitrial outlier in the northwestern part of the Srisailam sub-basin of the Cuddapah basin, Andhra Pradesh (Sinha et al., 1995).The uranium deposit in the Chitrial area rests with a pronounced unconformity over the ca. 2.5 Ga old basement granitoid rocks (Mukherjee et al., 2017) (mainly biotite-chlorite rich porphyritic granite and gneiss) of the Eastern Dharwar Craton (EDC) at the northwest fringe of the Cuddapah basin. Surface

radioactive anomalies along the basement granitoid led to the establishment of a sizeable uranium deposit by Atomic Minerals Directorate (AMD) in recent years.

While studying the unconformity-type Chitrial deposit, it is felt that systematic analysis of the deformation sequence of the granitoid massif, which hosts the deposit and evolved as a major component of the upper to middle crustal segments of the EDC under a protracted brittle to ductile deformation regime (Das et al., 2018), is essential. Proper evaluation of these internal deformation structures of the basement rocks and establishing the nature of overprinting relationships of structures and micro fabrics may contribute to the knowledge of the intrinsic processes responsible for their formation and that of the associated uranium-mineralization. The proposed Ph.D. programme thus aim to critically evaluate the structural history of the basement - cover rocks, establish the sequence of tectonic events and analyse the structural control behind uranium mineralization. The final aim is to develop a kinematic model of ore localization in the Chitrial area.

2. GEOLOGICAL BACKGROUND

The granitoid rocks of the Chitrial area belong to the large granitic province of the Eastern Dharwar craton (EDC), south India (Fig.1a). The EDC together with the Western Dharwar Craton (WDC) form the composite Dharwar craton of the southern Indian (Fig. 1a) crustal block that was stabilized at around ~2.51 Ga (Bhaskar Rao et al., 2008; Manikyamba and Kerrich, 2012; Dey, 2013; Mohan et al., 2013; Peucat et al., 2013; Santosh et al., 2015; Lancaster et al., 2015). Barring minor remnants of older (>3.0 Ga) TTG gneiss, the EDC principally comprises successive calc-alkaline to potassic intrusive granitoid (2.75 -2.51 Ga) bodies elongated in NNW-SSE direction with intervening sub-parallel, narrow, highly deformed greenstone belt successions (ca. 2.7-2.6 Ga; Jayananda et al., 2000, 2006, 2013; Chadwick et al.,

2000, 2007; Chardon et al., 2011; Sarma et al., 2012; Manikyamba and Kerrich, 2012; Dey, 2013; Mohan et al., 2013; Peucat et al., 2013; Santosh et al., 2015; Mukherjee et al., 2017).

N-S, NW-SE to NE-SW trending basic dyke swarms are prevalent within the granitoid massifs of the EDC which are dated at ca. 1.9-1.8 Ga (French et al., 2008; Anand et al., 2003). The dyke emplacement is presumed to coincide with opening of the Proterozoic Cuddapah basin (CB) along the eastern margin of the EDC (Fig. 1a; King, 1872; Nagaraja Rao et al., 1987; Saha and Tripathy, 2012; Patranabis-Deb et al., 2012; Collins et al., 2015; Sheppard et al., 2017). After initiation, the CB developed in three to four successive cycles (Nagraja Rao et al., 1987; Patranabis-Deb et al., 2012; Collins et al., 2015) depositing unconformity bound sequences of Papaghni-Chitravati Groups, Nalamallai Group, Srisailam Formation and Kurnool Group respectively. In the Chitrial area, the 2.51 Ga granitoid rocks form the basement over which the siliciclastic rocks of the ~1.66-1.59 Ga Srisailam Formation (third cycle; Collins et al., 2015) of the Cuddapah Supergroup was deposited with a prominent unconformity (Fig. 1b). The Srisailam Formation rocks occur as a small outlier – the Chitrial outlier, (Fig.1b) over the Neoarchean granitoid rocks of the EDC in the north-western fringe of the Srisailam sub-basin, Cuddapah basin. The unconformity plane between the basement granitoids and the overlying Srisailam quartzite (Fig.1c) is very well exposed in hilly road sections on way to the Chitrial village. The prominent map scale WNW-ESE trending Dindi lineament marks the southern limit of the Chitrial outlier. The Chitrial area is important for uranium mineralization within the basement granitoid and along its contact with the overlying rocks of the Mesoproterozoic Srisailam Formation (Verma et al., 2009; Bhoopathi et al., 2013). Subsurface exploration by AMD led to further subdivision of the area into five blocks (Fig.1b) (Main block, Block 1, Block 2, Block 3

and Block 4) according to uranium concentration and delineation of a mineralized 'Main Block' north of the Chitrial village.

3. OBJECTIVES

1. Critical evaluation of the structural history of the basement and cover rocks.
2. Develop an idea about the nature of ore mineralization and its mode of occurrence.
3. Understanding the succession of tectonic events controlling mineralization and emplacement.
4. Reconstructing the overall tectonic cum deformational set-up of the basement-cover sequence in order to predict the vertico-lateral extension of the uraniferous horizons.
5. Elucidating structural control in the localization of uranium mineralization and predicting the possibility of uranium mineralization in similar basement-cover contacts.

4. METHODOLOGY

1. Orientation data of mesoscopic structural elements were collected systematically from the basement granitoids rocks (Fig.2a) of the entire study area and were plotted in orientation diagrams for deformation (Fig.2b-e) and kinematic analyses. For establishing the sequence of formation of deformation structures and the chronology of deformation, large scale structural maps (Fig.2f) in 1:50m scale have been prepared from selected areas to document overprinting relationships of successive fabric elements (Table.1).
2. Analysis of fault slip data was carried out to yield a statistically stable tensor solution (Arlegui- Crespo and Simon-Gomez, 1998) using the computer program Win-Tensor to estimate the orientation of both the maximum and minimum principal stress axes during the D4-D5 brittle deformation episodes. A minimum number of 20 data per site are

sufficient for kinematic data visualization, processing, and analysis. WIN-Tensor program uses the basic principle of tensor program, the 'Right Dihedron method' which was originally developed by Angelier and Mechler (1977) as a graphical method for the determination of the range of possible orientations of σ1and σ3 stress axes in fault slip analysis (Delvaux and Sperner, 2003). Individual raw data of conjugate fracture set orientations from each location have been used in the Tensor program to determine the orientation of the principal stress axes (σ1, σ2 and σ3).

3. For microstructure and SPO measurement, oriented rock specimens were collected and 81 numbers of thin sections were prepared to study and analyse the deformation microstructures. It facilitated the estimation of the intensity and mechanism of deformation phases and the deformation temperature during D1-D3 phases in particular. Microstructure was analyzed with a *Nikon Eclipse LV100POL* optical microscope. The intensity of shape preferred orientation (SPO) of mica, quartz and feldspar grains are determined separately from 12 foliated granitoid samples (Table.2).
4. For crystallographic preferred orientation (CPO) measurement, the EBSD Electron Back-Scattered Diffraction (EBSD) analysis has been performed on 4 selected granite mylonite specimens (Table. 3). Thin sections were prepared by cutting the samples perpendicular to the foliation plane (S3) and parallel to the stretching lineation (L3; XZ plane) in the laboratory of department of Geology, Presidency University, Kolkata. The prepared thin sections were polished chemically using colloidal silica for four hours to remove the damaged layers on the surface. The samples were set on a 70^{O} pre-tilt holder with respect to the incident electron beam. To understand the textural evolution under high-magnification the Backscatter Electron Images (BSI) of the thin-sections were taken

using a JEOL JSM-6390. A Scanning Electron Microscope (SEM) equipped with a JED-2300 Energy Dispersive System (EDS) in the department of Earth and Planetary Systems Science, Hiroshima University, Japan. The operating voltage was fixed at 15kV during the qualitative analysis. EBSD pattern were also generated with accelerating voltage of 15 kV and data acquired using CHANNEL 5.0 software of Oxford Instruments HKL was used to index the generated CPO pattern. The pole figures were plotted in equal area stereographic diagrams with the trace of the mylonitic foliation (S3) and stretching lineation (L3) as reference directions.

5. For estimation of differential stress, 14 oriented specimens of mylonites were selected for preparation of thin sections perpendicular to S3 and parallel to L3, which were studied under *Nikon Eclipse LV100POL* trinocular microscope. The *NIS Elements D3.2* software was used to digitize the boundaries of recrystallized quartz grains (500-750 per thin section) and to automatically calculate their equivalent diameters. The recrystallized grains inside the clusters were selected for digitization avoiding those occurring along the fringes of the clusters in contact of feldspar grains or mica bands, as their growth may be inhibited by the presence of the other mineral phases (Passchier and Trouw, 2005). The piezometer of Twiss (1977) and Stipp and Tullis (2003) were then applied to calculate the differential stress from the measured equivalent grain diameters (Table.4).

6. Anisotropy of Magnetic Susceptibility (AMS) data acquired from the investigated granitoid samples are presented in Table. 5. AMS analysis was performed on oriented granitoid samples. A total of 180 specimens were produced from 31 samples collected from 28 sites in and around the Chitrial outlier. Most of the samples collected are from the massive variety of the granitoid while 3 samples were collected from the

foliated granitoid (Table. 5). The measurements were made on cylindrical cores in spinner mode using the KLY-4S Kappabridge (AGICO, Czech Republic) at the AMS laboratory of Department of Geology & Geophysics, Indian Institute of Technology, Kharagpur, India. For statistical treatment of AMS data, the oriented granite samples were drilled to produce multiple cylindrical cores (25.4 mm in diameter X 22 mm in height). Each core was analyzed in three different directions to get the various AMS parameters using the program SUFAR. Total 180 cores (minimum 5 cores per sample) were analyzed and mean value of each sample was calculated by the program Anisoft (version 4.2, AGICO). The mean susceptibility (K_m) for each core and the magnitude and orientation of the three principal axes of the magnetic susceptibility ellipsoid, viz. K_1, K_2 and K_3 were obtained along with other parameters such as magnetic foliation (F), magnetic lineation (L), corrected degree of anisotropy (P_j) and shape (T).

Temperature variation of magnetic susceptibility (κ - T) analysis was carried out from 4 granite specimens in order to identify the dominant minerals contributing in AMS of which two specimens (CT 207 & CT 210) were having low susceptibility $K_m<500 \times 10^{-6}$ and two (CT 206 & CT 220) having high susceptibility $K_m>500X10^{-6}$ (Table.5). The specimens were analyzed using Kappa Bridge KLY-2 attached with CS-3 in the magnetic laboratory of Indian Institute of Geomagnetism, Allahabad, India.

5. STRUCTURAL ANALYSIS FROM BASEMENT GRANITOID ROCKS

The granitoid rocks of the study area present a polyphase deformation history (Table.1) reconstructed on the basis of detailed structural analysis incorporating interrelations of styles and orientations of structural elements from rock outcrops (Fig.2a). The analysis reveals that the granitoid rock suite, comprising massive (Fig.3a), porphyritic (Fig.3b) and gneissic varieties, is

characterized by at least five (D1-D5) structure-forming events: (1) poorly exposed D1-D2 structures probably formed in end-Archaean transpressive deformation resulting from oblique convergence of EDC with WDC at ca. 2.51 Ga (2) mesoscopic conjugate shear zone development resulting from NW-SE strike parallel compression – D3 (3) Later brittle event(s) (D4-D5) marked by faulting and fracturing of granitic-gneissic rocks and granite-gneiss plus overlying Srisailam Formation rocks respectively (Fig.3c).

i) D1-D2 deformation:

A gneissic layering (S_1) is observed in isolated pockets dispersed within the prevailing granitic country rock displaying massive to porphyritic character in the area. The gneissic layering (S_1) is dominantly NW-SE trending with vertical to sub-vertical (Mean orientation $325^o/89^oW$; Fig.2b) dip and is marked by alternate quartzo – feldspathic and mafic bands. The S1 is subjected to tight folding (Fig.3d) (D_2) at places with a secondary incipient foliation (S_2) developing axial planar to the NW trending folds. The S_2 foliation, defined by parallel arrangement of flaky biotite grains, show similar NW-SE trend as the S_1 layering (Fig.3e). Assuming the gneissic layering to be a product of early deformation D1, it's later folding and development of the S2 foliation has been marked as a later phase of deformation D2 in this study.

ii) D3deformation:

The D3 deformation is manifested in conjugate ductile shear zone (dsz) development in gneisses as well as in massive and porphyritic varieties with associated mylonitic foliation (S3; Fig. 2c,d) and lowly plunging stretching lineation L3. The dszs are restricted to narrow bands of 2-3meter to few cm width and limited strike extent. TheS3 is defined by stretched feldspar

augens showing recrystalized tail and quartz ribbon embedded in a fine grained quartz-feldspar-biotite rich matrix locally grades to ultramylonites in dszs. Two different orientation of S3 foliations are found, N-NNE (mean orientation197^{o}/88^{o} W; Fig.2c) shear zones consistently give sinistral shear sense (Fig.3f) while E-WNW (mean orientation 098^{o}/90^{o}; Fig.2d) give dextral (Fig.3g). This later mylonitic foliation (S_3) transects both the S2 foliation (Fig.3h) and S1 layering at low angle (Fig.3i). Both the NNE and WNW trending S3 foliation make an obtuse angle of 99° between themselves from which the direction of maximum compression (σ1) can be determined (Ramsay and Huber1987) to be lying in the NW-SE quadrant (327.5^{o}-147.5^{o}; Fig. 2e).TheS3 fabrics also include development of S-C fabrics, asymmetric kinks, minor asymmetric fold in the associated pegmatite, quartz and epidote veins, and recrystallized tails on large feldspar clasts showing σ-type tails (Fig.3f, g). Mean orientation of L3 varies from 015°→195° to101°→281°for the NNE-SSW (Fig.2c) and E-W trending (Fig.2d) S3 planes (dsz sets) respectively.

iii) Brittle deformation phases(D4-D5):

Two phases of brittle deformation are distinct from the area. The earlier one (D4) is restricted to the granitoid and gneissic rocks of the area while the later one (D5) affects both the basement rocks as well as the overlying younger rocks of the Srisailam Formation. Accordingly these have been clubbed into Pre-Srisailam and Post-Srisailam brittle deformation phase structures respectively.

(a) Pre-Srisailam brittle deformation phase structures (D4):

Developments of conjugate strike slip faults in mesoscopic scale within gneisses as well as massive and porphyritic granitoids characterize the D4 phase. Vertical conjugate strike slip faults of limited strike extent and varying orientations (N-S, E-W, NNE-SSW, ENE-WSW

and WNW-ESE) have profusely developed in many places in the granitoid massif in outcrop scale. The faults show clear offset o f the gneissic layering S1 (Fig.3j), the mylonitic foliation S3 (Fig.3k) developed during D1-D3 phases as well as the intrusive basic dykes present in the area. This later brittle episode is manifested by the development of narrow (cm to mm thick) breccia horizons (Fig.3l), consisting of breccias – cataclasites and presenting chlorite-opaque enrichment and local solution effects along irregular clasts boundaries.

The orientation measurements of mesoscopic faults are made from 84 stations in the granitoid massif outcrop from the study area. The change in orientation of the conjugate shear planes indicate that the maximum principal stress direction instrumental behind mesoscopic-scale conjugate fracture generation also varied in space during deformation. Systematic measurement of the brittle shear fractures over the entire terrain establish that the conjugate shear planes occur in different sub-sets and orientation of the sub-sets changes in different parts of the area. The conjugate faulting (Fig.3j; D4 phase) is characterized by the association of dextral strike slip faults striking variously around N10-N350 (mean orientation 183°/90°;Fig.4a) and N15-N50 (mean orientation 039°/90°; Fig.4b).The corresponding conjugate sinistral ones also present various strike orientations ranging around N60-N85 (mean orientation 082°/89°N; Fig.4a) and N90-N110 (mean orientation 100°/89°S; Fig.4b). The major principal stress$\sigma 1$ deduced from the bisector of the dihedron composed by the vertical conjugate sets is horizontal with azimuth varying between 039.5°- 069.5°, i.e., lying dominantly in the NE-ENE quadrant (Fig. 4a,b). The E-W to N110 trending sinistral set is the more dominant among the conjugate sets. Data analyzed through the Win-Tensor program also establishes that the conjugate shear planes occur in different sub-sets of variable orientations (Fig.4c-g). The orientation diagrams

indicate that the maximum principal stress direction was dominantly horizontal and varied between NNE-SSW to NE-SW directions.

An attempt was also made to ascertain the dominant fracture set in individual mineralized blocks as identified by geologists from AMD. For this purpose, both fracture counting per unit square meter in outcrop volume as well as orientation of individual fractures were noted from more than 200 sites in and around the five mineralized blocks and block wise rose diagrams have been prepared (Fig.4h-k). It is observed that amongst the five prominent fracture sets (N–S, E – W, NNE–SSW, ENE – WSW and WNW–ESE), the dominant trend of fracture is WNW – ESE trending in the Main Block (Fig.4h, whereas in other blocks, such as in Block 1 the dominant set is NNE – SSW (Fig.4i) and ENE – WSW while in Block 4, the dominant trend of fractures is NNE – SSW (Fig.4k). Fig.4j depicts dominant fracture set orientation in the adjacent Block 2 which is dominantly in NNE-SSW direction.

(b)Post-Srisailam brittle deformation phase structures (D5):

This phase is characterized by development of WNW-ESE trending faults that displace the basement granitoid-Srisailam Formation unconformity surface (Fig. 5). The Dindi lineament is interpreted to be one such megascopic structure that displaces the granite-Srisailam Formation unconformity surface, in an apparent dextral sense (Fig. 5). Similarly the Atmakur Fault, developing along the southern margin of the Srisailam basin (Fig. 5), can be clubbed under the category of D5 faults in the terrain. N-S, E-W, NE-SW and WNW-ESE trending faults are locally common in mesoscale within the sandstone outcrops. Effect of faulting within sandstone outcrops, is also pronounced with steepening and sudden change in bedding orientation as well as local brecciation and fracture plane development. In the underlying granitoid massif, evidence of this phase of brittle faulting is represented by reactivation along earlier (D4) faults and

fracture surfaces. N-S and E-W to NW-SE trending joint sets are also common in the granitoid massif, which probably formed during the D5 deformation episode.

6. MICROSTRUCTURAL STUDY

The Chitrial granitoid body dominantly comprises quartz, K-feldspar, plagioclase and biotite with chlorite, apatite, allanite, epidote, magnetite and zircon present as accessories. Observed microfabrics and microstructures are interpreted to have developed as a result of initial high-T magmatic to submagmatic crystallization followed by D1-D3 ductile and D4 brittle deformation phases (Table. 1), which is elaborated below sequentially.

6.1. Magmatic fabric

The granite shows quartz-feldspar interlocking texture (Fig.6a) or an inequigranular porphyritic texture where feldspar is present as phenocrysts embedded in quartz-biotite rich groundmass. Chessboard subgrain pattern in quartz (Fig. 6a) indicate magmatic crystallization in the stability field of high-T quartz (Kruhl, 1996). Locally plagioclase show deformation twins and kinking but recrystallization or other deformation features are absent. The rims of K-feldspar crystals are replaced by myrmekite (Fig. 6b).

6.2. D1-D2 deformation

The gneissic layering (S1) consists of quartz-plagioclase rich and biotite rich layers (Fig. 6c). Oriented biotite and flat faces of recrystallized quartz and feldspar lenses define the main schsistosity (S2). Gneissic layering (S1) and S2 are mostly parallel. Dynamic recrystallization of quartz by bulging and subgrain rotation is very common while feldspar show wavy extinction and deformation band structures implying temperature of deformation to be at 400-450^{o}C. Bending and kinking of biotite flakes is a common feature at microfold hinges.

6.3. D3 deformation

The most prominent microstructure in D3 is a mylonitic foliation S3 which develops within the gneisses as well as within the massive and porphyritic granitoids. S3 is defined by very fine grained matrix of quartz and feldspar, quartz ribbon, stretched sub-elliptical feldspar crystals and oriented biotite flakes (Fig. 6d, e) with a dominant mineral assemblage of quartz-plagioclase-K-feldspar-biotite ± magnetite. The sense of shear is deduced from S-C fabrics, feldspar σ-δ clasts and local flexures. It is observed that sinistral shear is predominant in S3 having NNE-NE trend (Fig. 6d) while dextral sense of shearing is prevalent in S3 having WNW-ESE trend (Fig. 6e). Quartz in D3 fabrics shows long ribbon shaped grains or aggregate of small elongated recrystallized grains with features indicating recrystallization by grain boundary migration and/or subgrain rotation. Feldspars show a wide range of deformation fabrics that include kinking of deformation twins (Fig. 6f) and recrystallization producing core and mantle structures (Fig. 6g) as well as recrystallized tails suggesting minimum deformation temperature to be well above 650^{o}C (Tullis and Yund, 1991).

6.4. D4 deformation

Development of fractures and cataclasite zones in gneisses and massive (Fig.6h) and porphyritic granitoids characterize the D4 phase in grain-scale. The gneissic foliation (S2) and mylonitic foliation (S3) get displaced by D4 intra- to inter-granular fractures (Fig.6i) of varying orientations, which get connected with each other to form thorough going fractures which eventually lead to cataclasis and development of thin to thick cataclasite horizons / crush zones. Angular grains of quartz and feldspar of variable sizes are present within such zones The fractured zones marked by brecciation usually display a sharp contact with the host rock (Fig. 6j) and often grades to complete pulverized rock (Fig. 6k). Extensive alteration and development of

solution seams is observed in such damage zones, which include chlorite (after biotite), sericite (after plagioclase) and epidote. Cataclasites display rotated polycrystalline fragments separated by a weak foliation, made up of dark layers of fine grained opaques, chlorite and crushed quartz-feldspar, in the matrix developing parallel to the shear boundaries and wrapping larger clasts. The development of chlorite rich zones plus widespread cataclasis of quartz-feldspar with localized solution effects along D4 microfaults indicate a possible temperature of deformation to be 200-250°C. Uranium mineralization is observed within fractured and veins within granite (Fig.6l). Mineralization is also observed along with biotite and chlorite in some granite.

6.5. Shape Preferred Orientation (SPO) analysis

The intensity of SPO is measured from selected samples of both the S1-S2 and S3 fabric zones separately. Again from each fabric zone, SPO corresponding to mafic mineral (κ_{mf}), quartz (κ_{mf}) and feldspar (κ_{mf}) fractions are determined separately and is represented in Table 2. It is observed that SPO (κ) values do not show significant variation in the two fabric zones. For mafic minerals, κ_{mf} values range from 1.6-2.29 to 1.5-2.21 in S1-S2 and S3 fabric zones respectively (Table. 2), barring sample no. CT205, which shows κ_{mf} value 5.24. Feldspar fraction shows a similar variation in the two fabric zones (κ_{fds} values range from1.41-2.49 to 1.28-2.21 in S1-S2 and S3 fabric zones respectively, Table. 2). For quartz, SPO intensity is slightly higher in S3 fabric zones (κ_{qtz}: 1.75-3.0) than in S1-S2 zones (κ_{qtz}: 1.44-2.13; Table.2).

6.6. EBSD analysis

Results of the CPO data are shown in Fig.7. Samples CT 8a and CT 7AS were collected from WNW trending dsz zones while CT 81 BT and CT 81 AS were from N-S trending dszs

(Table.3). The c-axis pattern in CT 7AS and CT 8A indicates a consistent dextral slip sense. In CT 8a, (Fig.7a) the fabric pattern suggests dominant deformation of quartz by dislocation creep on prism <a> slip and/or rhomb <a> slip while the pattern in sample CT 7AS (Fig.7b) clearly shows that dislocation creep in quartz was achieved through prism <c> slip. Similarly the c- axis pattern of CT 81BT and CT81AS clearly indicates sinistral slip sense (Fig.7c and 7d). Dextral and sinistral slip sense deduced from c-axis pattern from the D3 dsz domain (WNW and N) samples respectively is consistent with shear sense indicators observed from outcrop scale and microstructural analysis. The c-axis pattern also supports the deformation temperature achieved during D3 deformation.The c-axis pattern in sample CT 81BT (Fig.7c) show orthorhombic symmetry (Lister and Williams 1979; Simpson and Schimd, 1983; Schimd and Casey, 1986) and deformation of quartz by dislocation creep through a combination of basal <a> slip and rhomb <a> slip whereas for CT 81AS fabric pattern further indicates that dislocation creep in quartz was achieved principally through prism <c> slip. The quartz CPO patterns further indicate that the recrystallization of quartz was largely achieved through prism <c> slip lending support to the earlier contention from microstructural observations that the probable deformation to be lying above 600°C temperature during conjugate shearing and dsz development in D3 deformation. This high (>600°C) deformation temperature during D3 and inferred 400-450°C deformation temperature during D1-D2

6.7. Differential Stress Calculation

Average equivalent diameter (D) of recrystalized quartz from total 14 samples (both granite mylonite and strongly foliated granite) was measured with a Nikon Eclipse LV100POLtrinocular optical microscope using the NIS Elements D 3.2 software. The diameter of each recrystallized grain is defined by the diameter of the circle of same area. The grain

parameters were automatically measured by using the NIS Elements D 3.2 software. For statistical analysis eq. diameter of minimum 500 recrystallized quartz grains are measured from which average eq. diameter (D) for each samples have been calculated (Table.4). Then the value of D was used to measure the Differential stresses, both according to Twiss (1977) and Stipp and Tulis (2003) in each sample.

$$\Delta\sigma = BD^{-p}$$

Where $\Delta\sigma$ = Steady state differential stress; D = recrystalized eq. grain diameter; B and P are empirical constant. According Twiss (1977) and Stipp and Tullis (2003) the value of B = 677.42; 668.95and p = 0.68; 0.7936 respectively. Oriented samples of granites were used for differential stress ($\Delta\sigma$) studies (Table.4). The minimum and maximum values of differential stress obtained from the piezometer of Twiss (1980) is 29 Mpa and 95 Mpa respectively while that of Stipp and Tullis (2003) gives the minimum and maximum values are 15 Mpa and 68 Mpa respectively.

7. **ANISOTROPY OF MAGNETIC SUSCEPTIBILITY STUDY**

The majority of the analyzed samples (26) present mean bulk susceptibility (K_m) values below <500 X 10^{-6} SI unit, which indicate, following Bouchez (1997), that the granitoids of the Chitrial area is dominantly paramagnetic in nature. However, remaining 5samples show K_m values between 1190-8630 X 10^{-6} SI unit (Table.5, which implies that some of the granitoids are ferromagnetic in character (Bouchez, 1997). The magnetic foliation trajectory map (Fig.8) clearly shows that the computed magnetic foliation data forms two distinct clusters. The data are plotted separately in the orientation diagrams. Lower hemisphere equal area plots of K1, K2 and K3 axes of the analyzed cores from the granitoid samples are presented in Fig.8a,b.

Interestingly, a subset of the total data set which includes the 3 samples of the gneissic variety, yield a consistent NW trending magnetic foliation (Fig.8c) of mean orientation $313^o/90^o$ while the other subset yield a consistent NE trending magnetic foliation (Fig.8d) of mean orientation 039°/85°SE. The deduced NW trending ($313^o/90^o$) and NE trending ($039^o/85^o$SE) magnetic foliation sets are kinematically consistent with the deduced shortening directions, NE-SW and NW-SE based on orientations of observed mesoscopic structural elements (S1-S2planes–D1-D2and conjugate dszs and mylonitic foliation patterns –D3).

Also while preparing lower hemisphere equal area plots of magnetic lineation (K1), the data Fig.8e shows that the magnetic lineation data of NW trending magnetic foliation plane consistently plunge due SE at a low angle (10°→134°). However, it is clear from Fig.8f that the lineation pattern in NE trending magnetic foliation plane is about 21°→041°. Figs. 9a,b represent the Km vs. Pj and Pj vs. T plots for all the studied samples. The degree of magnetic anisotropy (P_j) varies from 1.009 to 1.49 (Table. 5) in granitoids while the shape parameter (T) ranges from –0.403 to 0.688 indicating that the samples fall in both the oblate and prolate susceptibility ellipsoid field (Fig.9b). The plot of Km vs. Pj (Fig. 9a) helps to assess the role of magnetic anisotropy (Km) behind degree of anisotropy (Pj). The ferromagnetic granitoids with high K_m values in general show higher P_j values (Table.5).

Temperature variation of magnetic susceptibility (κ-T) analysis was carried out on some representative samples (4 granite samples) (Fig.9c-f) to confirm presence of ferromagnetic minerals like magnetite in the granitoids. The samples were analyzed using Kappa Bridge KLY-2 attached with CS-3 in the magnetic laboratory of Indian Institute of Geomagnetism, Allahabad, India. It is observed that in samples (CT206 and CT220A) having $K_m$values > $500X10^{-6}$ SI unit, temperature variation curve show significant drop in magnetic susceptibility at 580^oC Curie T of

magnetite) in the heating experiment (Fig.9c, d). On the other hand, in samples (CT207 and CT205) having $K_m$values <500X10^{-6}SI unit, no appreciable drop in magnetic susceptibility values are observed during heating and cooling indicating dominance of paramagnetic minerals (Fig.9e, f).

Ore petrographic studies (Fig.9g), BSE images (Fig.9h) and EDS analysis of the samples having high K_m value (>500X10^{-6} SI unit) further lend support to the presence of magnetite in contributing higher susceptibility (K_m) values in these samples. Magnetite has been observed to grow subparallel to the prevailing schistosity (S1-S2/S3; Figs. 9g-h) in the samples defined by mafic mineral phases as well as elongated quartz-feldspar. Thus it is inferred that though presence of magnetite has a strong control, particularly in the ferromagnetic samples, the ultimate magnitude of the AMS in most of the studied granitoid samples is a result of the combined contribution of the ferro-para and dia-magnetic mineral fractions (Yaouancq and Macleod, 2000; Rosière et al., 2001; Bascou et al., 2002; Raposo et al., 2006; Kratinova et al., 2010; Lamali et al., 2013; Silva et al., 2014; Ghosh et al., 2018).

8. DISCUSSION

i) Deformation history of the basement granitoid massif

The five-stage deformational history of the granitoid rocks at Chitrial is summarized in Table. 1. The dominant NW directed trend of the S1-S2 planes implies their formation under a protracted NE-SW directed compression. Regional considerations (Naha et al., 1993; Mukhopadhyay 1986; Beeriah et al., 2001; Chakrabarti et al., 2006; Matin, 2006; Mondal and Mamtani, 2013; Bhatt et al., 2017) suggest that D1-D2 were major events of W-NW directed folding and thrusting in EDC (Chadwick et al., 2003, 2007; Jayananda et al., 2006, 2008, 2013;

Chardon et al., 2008; Griffin et al., 2009; Meert et al., 2010; Sarma et al., 2011; Sengupta and Roy, 2012; Dey, 2013; Peucat et al., 2013).

The conjugate pattern of dszs, defined by sinistral NNE and E-W dextral sets, is consistent with a NW-SE (327.5°-147.5°) shortening to be dominant during D3 deformation. Thus a gross change in compression direction is observed from the earlier D1-D2 stage. A NW-SE directed shortening during D3 had been envisaged by workers from WDC-EDC, manifested in NE directed open folds, by conjugate fold development on S1-S2 (Naha et al., 1993; Mukhopadhyay 1986; Matin, 2006) or by refolding of F1-F2 folds and their plunge reversals on a regional scale (Naha et al., 1993; Mukhopadhyay 1986; Beeriah et al., 2001; Chakrabarti et al., 2006; Matin, 2006; Mondal and Mamtani, 2013; Bhatt et al., 2017). However, most of these reports showing effects of D3 on earlier structures are from the schist belts adjoining the granitoids and gneisses. The present study clearly depicts that the granitoids of the study area accommodated the D3 NW'ly shortening by widespread development of conjugate shear zones (dszs) in mesoscopic scale.

A later conjugate set of brittle faults and shear fractures of D4 generation overprint and displaces the ductile dsz structures of D3, the S1-S2 planes as well as the intrusive basic dykes within the granitoids. These conjugate brittle structures developed under dominant D4 phase ENE compression (039.5°-069.5°) are confined within the granitoid outcrops only and are absent from the overlying outcrops of the Srisailam Formation.

The last D5 phase structures are marked by some large WNW trending sub-vertical faults, e.g., the Dindi lineament (Fig.5), in the area which often show map scale displacement of the basement granitoid-Srisailam Formation contact. Mesoscopic D5 stage N-S, NE-SW, E-W

and WNW-ESE trending faults and fractures are common within the overlying Srisailam Formation outcrop.

ii) AMS data and its tectonic significance

The magnetic foliation data of the studied granitoids show two distinct NW and NE trending sets. The NW trending magnetic foliation is found to be essentially parallel to the mesoscale planar structures of regional D1-D2 deformations and is thus correlated with the D1-D2 phases. On the contrary, the NE trending magnetic foliation appears to be kinematically compatible with the NW-SE compression direction deciphered from conjugate ductile shear zone patterns of the D3 event. The D3 structural domain presents more spread in magnetic foliation orientation varying from N-S, NE-SW, NNE-SSW, E-W to WNW-ESE with mean orientation of foliation being NE-SW ($039^o/85^oSE$). It may be reconciled here that the D3 ductile deformation episode is marked by conjugate mesoscale shear zone (dsz) and mylonitic foliation (S3) development having mean orientations NNE-SSW (197°/89°W) and ENW-WSE (098°/90°). The conjugate orientation pattern of the dszs was used to deduce the major shortening direction ($\sigma1$) of D3 deformation episode to be NW-SE (347.5°-147.5°) trending. The NE-SW trend ($039^o/85^oSE$) of the mean orientation of the magnetic foliation data from samples of the D3 structural site is significant in this respect. It appears that the NE-SW magnetic foliation data is kinematically compatible with the observed conjugate dsz pattern in the granitoid and implies their formation under the bulk NW-SE shortening episode (347.5°-147.5° trending $\sigma1$) that is also characteristic of the D3 deformation phase and formation of the conjugate dszs. Hence, it can be concluded that the development of magnetic fabrics in the granitoid rocks of the Chitrial area is essentially tectonically controlled and represent the successive D1-D2 and D3 deformation episodes which are regionally pervasive within the EDC.

iii) Structural control of Uranium mineralization

Surface radiometric survey by AMD have delineated significant uranium mineralization in Chitrial outlier. Uraniferous occurrences are mainly associated with the basement granitoids while some of it is also recorded in the overlying Srisailam sandstones close to the unconformity plane. More than 90% of the main ore body occurs in granitoid at varying depths of 3 to 82m in the mineralized main block. Though the ore body appears as a blanket along the unconformity surface, the rich mineralized zones preferentially occur along WNW-ESE and N-S trending fracture zones. It has been observed that these fractures and their intersections are locales of high grade mineralization (Ramesh Babu et al., 2010, 2012; Rajaraman et al., 2011).

From the field survey and systematic measurement of fractures from nearly 200 sites around the mineralized blocks, it has been concluded that the fracture density is higher in the Main Block. The area surrounding the main block of uranium deposit contains a Neoarchaean basement reworked during Proterozoic and later times. Plotting of fracture orientations in the rose diagrams reveal the WNW-ESE trending fracture set to the dominant set in this block with the N-S set as the second dominant one. The uranium ore body in the main block occurs in two sectors separated by a N-S trending fault (Rajaraman et al., 2011) and are bounded to the north and south by WNW-ESE trending faults. The regional fault structure in the vicinity is the WNW-ESE trending Dindi lineament which developed as a D4 stage fault, rejuvenated during D5. Several population of D4-D5 stage faults have been mapped in the host rock surrounding the main block. The characteristics and orientations of faults indicate that, like the regional Dindi lineament, these are also mostly D4 stage faults reworked in D5 times.

In surface outcrops rare uranium shows are always associated with narrow veins occupying thin fractures in breccia and cataclasite zones. Thin sections of surface and borehole samples reveal occurrence of uranium and sulfide minerals in narrow veins, cataclasite zones and

intergranular spaces. The principal group of mineralized fracture zones strikes N-S and WNW-ESE and corresponds to the principal systems of D4 stage fractures which were rejuvenated during D5 stage event. Based on cross-cutting relationships and textures observed in thin sections and BSE images, the paragenesis of the mineralized deposit has been described in seven stages of which the 3rd, 5th and 7th stages are uraniferous which alternate with a combination of sulfide and iron oxide mineralization stages (Mukherjee et al., *in prep*.). It indicates existence of recurrent hydrothermal activity and/or tectonic pulses to be ultimately linked with mineralization in the area.

As per mode of occurrence, the uranium ores are concentrated in two dilational zones/ jogs north of the regional Dindi lineament and bounded by second order N-S and WNW-ESE trending faults. The D4 faults were reactivated in these dilational areas. During D5, the faults with suitable orientation to the stress state were opened and the rest were closed. Working out of the tentative orientation of the stress field during D5 allows to predict the range of fault surfaces with suitable orientation for mineralization. It shows that the WNW-ESE and N-S trending faults and fractures were invariably open in contrast to the fault orientations in the stretching field and the latter were thus not mineralized at all. Therefore the NE-NNE oriented faults and fractures were closed during D5 while the WNW trending faults mostly opened up. This model is highly consistent with distribution of the uranium mineralized zone in the main block and strongly supports the validation of the proposed genetic model. The established stress regime can be tentatively correlated with N-S to NW-SE extension and probable opening of the adjoining Srisailam sub-basin. Reactivation of some of the large faults affecting the overlying Srisailam Formation indicates resurgence of brittle tectonics that affected the basement and basin in-fill as a whole. Such repeated tectonic pulses in continental interior are in conformity with multiple

deformation events recorded from the Cuddapah rocks under the influence of far-field stresses operating along basin margin.

9. CONCLUSIONS

Five compressive deformation phases (D1-D5) have been identified from structural analysis of the granitoid rocks of the study area. Of these, while the first three deformation phases (D1-D3) are ductile in nature, the latter two phases (D4-D5) are essentially brittle in characteristics. The D1-D2 phases are represented by gneissic layering (S1) development followed by isoclinal folding (F2) of S1 and development of axial planar S2 under a dominant NE-SW compressive event. The D3 ductile phase is represented by outcrop-scale conjugate ductile shear zone (dsz) development having sub-vertical attitude and associated mylonitic foliation (S3) development. The dszs with sinistral slip sense have a preferred NNE strike whereas the dextral slip dszs are dominantly showing WNW trending azimuth. The bisector of the obtuse dihedral angle gives the trend of the main principal stress direction to be NW-SE (327.5°-147.5°), which is nearly orthogonal to the deduced NE trending compression direction of the D1-D2 phases. In microscale, the D3 phase dszs are characterized by mylonitic-ultramylonitic fabric development, recrystallization of feldspar and biotite enrichment, which collectively indicates a deformation temperature above 600°C. The quartz CPO pattern also attest to this high grade (>600°C) deformation T during D3.These D1-D3 ductile phases are well described from both the EDC and WDC and are conceived to have resulted from ~2.51 Ga oblique collision of EDC island arc system against the stable shelf of the WDC. The D4 phase brittle structures are mainly represented by strike slip fault development in mesoscopic scale within granitoid rocks. These shear structures are distributed along conjugate planes with 40-60°

dihedral angle. The bisectors give the orientation of σ1 to be lying in the NE to ENE quadrants (039.5°-069.5°). In microscale, the D4 phase is represented by cataclasis, development of solution seams and chlorite-sericite enrichment along fracture surfaces indicating nearly ~200-250°C of deformation temperature. The D1-D4 phase structures have developed ubiquitously within the granitoid basement rocks of the study area. The D5 phase brittle faults on the other hand displaces the granitoid-Srisailam Formation contact indicating their post-Srisailam Formation evolution.

Funding

A part of this dissertation was carried out from the funding of Board of Research in Nuclear Science (BRNS), Department of Atomic Energy (DAE), Government of India (Project No. : 2011/36/59-BRNS/2186).

References

Anand et al., 2003 Anand, M., Gibson, S. A., Subbarao, K. V., Kelley, S. P., Dickin, A. P., 2003. Early Proterozoic Melt Generation Processes beneath the Intra-cratonic Cuddapah Basin, Southern India. Journal of Petrology 44, 2139-2171.

Angelier, J.T. and Mechler, P., 1977. Sur une methode graphique de recherche des contraintes principales egalement utilisables en tectonique et en seismologie: la methode des diedres droits. Bulletin de la Société géologique de France 7(6), 1309-1318.

Arlegui-Crespo, L.E., Simón-Gómez, J.L., 1998. Reliability of palaeostress analysis from fault striations in near multidirectional extension stress fields. Example from the Ebro Basin, Spain. Journal of Structural Geology 20(7), 827-840.

Bascou, J., Tommasi, A., Mainprice, D., 2002. Plastic deformation and development of clinopyroxene lattice preferred orientations in eclogites. Journal of Structural Geology 24, 1357-1368.

Beeriah, M.B., Sengupta, S., Venkataswami Ramachandran, T.V., 2001. Exploration for gold in sulphide ice banded magnetite chert band of Nagavie Malasamudra area, Gadag schist belt. Special Publication Geological Survey of India 58, 339-344.

Bhaskar Rao, Y.J., Vijaya Kumar, T., Krishna, K.V.S.S., Tomson, J.K., 2008. The Emerging Pattern of Crust formation and Recycling History in the Precambrian Dharwar Craton and the southern Granulite Terrain, Southern India: Constraints from Recent Geochronological and Isotopic Results. Memoir Geological Society of India 74, 147-168.

Bhatt, S., Rana, V., Mamtani, M. A., 2017. Deciphering relative timing of fabric development in granitoids with similar absolute ages based on AMS study (Dharwar Craton, South India). Journal of structural Geology 94, 32-46.

Bhoopathi, V., Niranjan Kumar, S., Sastry, R.S.N., Sinivas, B., Ramana Kumar, M., 2013. Delineation of Target Zones for Detailed Uranium Exploration Using Secondary Dispersion Haloes (Pedogeochemical) as a Tool in the NNW Parts of Srisailam Sub Basin, Andhra Pradesh (India). International Journal of Scientific and Research Publications 3, 1-10.

Bouchez, J.L., 1997. Granite is never isotropic: an introduction to AMS studies of granitic rocks. In: Bouchez, J.L., Hutton, D.H.W. Stephens (Eds.), Granite: from Segregation of Melt to Emplacement Fabrics. Kluwer Academic Publishers, Dordrecht, 95-112.

Chadwick, B., Vasudev, V. N., Hegde, G. V., 2000. The Dharwar Craton, southern India, interpreted as the result of late Archaean oblique convergence. Precambrian Research 99, 91-111.

Chadwick, B., Vasudev, V. N., Hegde, G. V., 2003. The Chitradurga schist belt and its adjacent plutonic rocks, NW of Tungabhadra, Karnataka: a duplex in the Late Archaean convergent setting of the Dharwar Craton. Journal Geological Society of India 61, 645-663.

Chadwick, B., Vasudev, V. N., Hegde, G. V., Nutman, A., 2007. Structure and SHRIMP U/Pb ages of granites adjacent to the Chitradurga schist belt: Implications for Neoarchaean convergence in the Dharwar Craton, southern India. Journal Geological Society of India 69, 5-24.

Chakrabarti, C., Mallick, B.S., Pyne, T.K., Guha, D., 2006. A Manual of the Geology of India. Geological Survey of India, Kolkata.

Chardon, D., Jayananda, M., Chetty, T. R. K., Peucat, J.J., 2008. Precambrian continental strain and shear zone patterns: South Indian case. Journal of Geophysical Research 113, B08402. https://doi. org/10.1029/2007JB005299.

Chardon, D., Jayananda, M., Peucat, J.J., 2011. Lateral constrictional flow of hot orogenic crust: Insights from the Neoarchean of south India, geological and geophysical implications for orogenic plateaux. G3- Geochemistry, Geophysics, Geosystems 12 (Q02005). https://doi.org/10.1029/2010GC003398.

Collins, A. S., Patranabis-Deb, S., Alexander, E., Bertram, C. N., Falster, G. M., Gore, R. J., Mackintosh, J., Dhang, C. P., Saha, D., Payne, J. L., Jourdan, F., Backe, G., Halverson, G. P., Wade, B. P., 2015. Detrital mineral age, radiogenic isotopic stratigraphy and tectonic significance of the Cuddapah Basin, India. Gondwana Research 28, 1294-1309.

Das, P., Mukherjee, S., Das, K., Ghosh, G., 2018. Integrating AMS data with structural studies from granitoid rocks of the Eastern Dharwar Craton, south India: Implications on successive fabric development and regional tectonics. https://doi.org/10.1016/j.jsg.2018.10.007.

Delvaux, D., Sperner, B., 2003. Stress tensor inversion from fault kinematic indicators and focal mechanism data: the TENSOR program. New insights into structural interpretation and modelling 212, 75-100.

Dey, 2013 Dey, S., 2013. Evolution of Archean crust in the Dharwar craton: the Nd isotope record. Precambrian Research 227, 227-246.

French, J.E., Heaman, L.M., Chacko, T., Srivastava, R.K., 2008. 1891–1883 Ma Southern Bastar–Cuddapah mafic igneous events, India: a newly recognized large igneous province. Precambrian Research 160, 308–322.

Ghosh, B., Das, P., Sarkar, D. P., Ghosh, G., Mukhopadhyay, J., Ando, J. I., 2018. Coalescing microstructure and fabric transitions with AMS data in deformed limestone: Implications on deformation kinematics. Journal of Structural Geology, https://doi.org/10.1016/j-jsg.2017.012.16.

Griffin, W. L., Kobussen, A. F., Babu, E. V. S. S. K., O'Reilly, S. Y., Norris, R., Sengupta, P., 2009. A trans lithospheric suture in the vanished 1-Ga lithospheric root of South India: evidence from contrasting lithosphere sections in the Dharwar Craton. Lithos 112, 1109-1119.

Jayananda, M., Moyen, J.F., Martin, H., Peucat, J.J., Auvray, B., Mahabaleshwar, B., 2000. Late Archean (2550–2520 Ma) juvenile magmatism in the Eastern Dharwar Craton, southern India: Constrains from geochronology, Nd–Sr isotopes and whole rock geochemistry. Precambrian Research 99, 225-254.

Jayananda, M., Chardon, D., Peucat, J.J., Capdevila, R., Martin, H., 2006. 2.61 potassic granites and crustal reworking, western Dharwar Craton (India): Tectonic, geochronologic and geochemical constraints. Precambrian Research 150, 1-26.
Jayananda, M., Kano, T., Peucat, J.J., Channabasappa, S., 2008. 3.35 Ga komatiite volcanism in the western Dharwar craton: constraints from Nd isotopes and whole rock geochemistry. Precambrian Research 162, 160-179.

Jayananda, M., Peucat, J.J., Chardon, D., Krishna Rao, B., Fanning, C. M., Corfu, F., 2013. Neoarchean greenstone volcanism and continental growth, Dharwar Craton, southern India: Constraints from SIMS U–Pb zircon geochronology and Nd isotopes. Precambrian Research 227, 55-76.

Jefferson C.W., Thomas D.J., Gandhi S.S., Ramaekers P., Delaney G., Brisbin D., Cutts C., Quirt D., Portella P., and Olson R.A., 2007. Unconformity associated uranium deposits of the Athabasca Basin, Saskatchewan and Alberta, in Goodfellow W.D. Ed., Mineral Deposits of Canada: A Synthesis of Major Deposit-Types, District Metallogeny, the Evolution of Geological Provinces, and Exploration Methods: Geological Association of Canada, Mineral Deposits Division, Special Publication No. 5, 273-305.

King, W., 1872. On the Kudapah and Karnul formations in the Madras Presidency. Memoirs Geological Survey of India 8, 346.

Kratinová, Z., Ježek, J., Schulmann, K., Hrouda, F., Shail, R. K., Lexa, O., 2010. Noncoaxial K-feldspar and AMS subfabrics in the Land's End granite, Cornwall: Evidence of magmatic fabric decoupling during late deformation and matrix crystallization. Journal of Geophysical Research: Solid Earth, 115(B9).

Kruhl, J. H., 1996. Prism-and basal-plane parallel subgrain boundaries in quartz: A microstructural geothermobarometer. Journal of Metamorphic Geology 14, 581-589.

Lamali, A., Merabet, N., Henry, B., Maouche, S., Graine–Tazerout, K., Mekkaoui, A., Ayache, M., 2013. Polyphased geodynamical evolution of the Ougarta (Algeria) magmatic complexes evidenced by paleomagnetic and AMS studies. Tectonophysics 588, 82-99.

Lancaster, P., Dey, S., Storey, C.D., Mitra, A., Bhunia, R.K., 2015. Contrasting crustal evolution processes in the Dharwar craton: insights from detrital zircon U–Pb and Hf isotopes. Gondwana Research 280, 1361-1372.

Manikyamba, C., Kerrich, R., 2012. Eastern Dharwar Craton, India: Continental lithosphere growth by accretion of diverse plume and arc terranes. Geoscience Frontiers 3, 225-240.

Matin, A., 2006. Structural anatomy of the Kushtagi schist belt, Dharwar craton, south India—an example of Archaean transpression. Precambrian Research 147, 28-40.

Meert, J.G., Pandit, M.K., Pradhan, V.R., Banks, J., Sirianni, R., Stroud, M., Newstead, B., Gifford, J., 2010. Precambrian crustal evolution of Peninsular India: a 3.0 billion year odyssey. Journal of Asian Earth Sciences 39, 483-515.

Mercadier, J., Richard, A., Boiron, M.C., Cathelineau, M. and Cuney, M., 2010. Migration of brines in the basement rocks of the Athabasca Basin through micro-fracture networks (P-Patch U deposit, Canada). Lithos 115, 121-136.

Mohan, M. R., Piercey, S. J., Kamber, B. S., Sarma, D. S., 2013. Subduction related tectonic evolution of the Neoarchean eastern Dharwar Craton, southern India: New geochemical and isotopic constraints. Precambrian Research 227, 204-226.

Mondal, T.K., Mamtani, M.A., 2013. 3-D Mohr circle construction using vein orientation data from Gadag (southern India) - implications to recognize fluid pressure fluctuation. Journal of Structural Geology 56, 45-56.

Mukherjee, S., Ghosh, G., Das, K., Bose, S., Hayasaka, Y., 2017. Geochronological and geochemical signatures of the granitic rocks emplaced at the north-eastern fringe of the Eastern Dharwar Craton, South India: Implications for late Archean crustal growth. Geological Journal 53, 1781 – 1801.

Mukhopadhyay, D., 1986. Structural pattern in the Dharwar craton. Journal of Geology 942, 167-186.

Nagaraja Rao, B.K., Rajurkar, S.T., Ramalingaswamy, G., Ravindra Babu, B., 1987. Stratigraphy, structure and evolution of the Cuddapah basin. In: Purana Basins of Peninsular India. Memoir Geological Society of India 6, 33-86.

Naha, K., Srinivasan, R., Gopalan, K., Pantulu, G.V.C., Rao, M.S., Vrevsky, A.B., Bogomolov, Y.S., 1993. The nature of the basement in the Archaean Dharwar craton of southern India and the age of the Peninsular Gneiss. Proceedings Indian Academic Sciences- Earth Planetary Sciences 102, 547-565.

Passchier, C.W., & Trouw, R.A.J., 2005. Microtectonics (2nd Ed). Springer-Verlag Berlin Heidelberg.

Patranabis-Deb, S., Saha, D., Tripathy, V., 2012. Basin stratigraphy, sea-level fluctuations and their global tectonic connections—evidence from the Proterozoic Cuddapah Basin. Geological Journal47, 263-283.

Peucat, J. J., Jayananda, M., Chardon, D., Capdevila, R., Fanning, C. M., Paquette, J. L., 2013. The lower crust of the Dharwar Craton, south India: Patchwork of Archean granulitic domains. Precambrian Research 227, 4-28.

Rajaraman, H.S., Ramesh Babu, V., Dandele, P.S., Chavan, S.J., Achar, K.K. and Ramesh Babu, P.V., 2011. Using VLF-EM to delineate a fracture in basement granites for uranium exploration. The Leading Edge 1158 – 1161.

Ramesh Babu, P.V., Chavan, S.J., Srivastava, S.K., Nagendra Babu, G., Reddy, S.V.S., Niranjan Kumar, S., Basu, H., Rajaraman, H.S., Dandele, P.S. and Saravanan, R., 2010. Report on ore reserves of Chitrial main block. Unpublished Report, AMD, Hyderabad.

Ramesh Babu, P.V., Banerjee, R., Achar, K.K., 2012. Srisailam and Palnad Sub-Basins: Potential Geological Domains for Unconformity–Related Uranium Mineralisation In India. Exploration and Research for Atomic Minerals 22, 21-42.

Ramsay, J. G., Huber, M.I., 1987. The techniques of modern structural geology, 2: Folds and fractures. Academic Press, London.

Raposo, M. Irene B., Ian McReath , D'Agrella-Filho, Manoel S., 2006. Magnetic fabrics, rock magnetism, cathodoluminescence and petrography of apparently undeformed Bambui carbonates from São Francisco Basin (Minas Gerais State, SE Brazil): An integrated study. Tectonophysics 418, 111-130.

Rosière, C. A., Siemes, H., Quade, H., Brokmeier, H. G., Jansen, E. M., 2001. Microstructures, textures and deformation mechanisms in hematite. Journal of Structural Geology 23, 1429-1440.

Saha, D., Tripathy, V., 2012. Palaeoproterozoic sedimentation in the Cuddapah Basin, south India and regional tectonics: a review. Special Publications Geological Society of London 365, 161-184.

Santosh, M., Yang, Q. Y., Shaji, E., Tsunogae, T., Mohan, M. R., Satyanarayanan, M., 2015. An exotic Mesoarchean microcontinent: The Coorg Block, southern India. Gondwana Research 27, 165-195.

Sarma, D.S., Fletcher, I.R., Rasmussen, B., McNaughton, N.J., Mohan, M.R., Groves, D.I., 2011. Archean gold mineralization synchronous with late cratonization of the Western Dharwar Craton, India: 2.52 Ga U-Pb ages of hydrothermal monazite and xenotime in gold deposits. Mineral Deposita 46, 273-288.

Sarma, D. S., McNaughton, N. J., Belusova, E., Mohan, M. R., Fletcher, I. R., 2012. Detrital zircon U–Pb ages and Hf-isotope systematics from the Gadag Greenstone Belt: Archean crustal growth in the western Dharwar Craton, India. Gondwana Research 22, 843-854.

Schimd, S. M., Casey, M., 1986. Complete fabric analysis of some commonly observed quartz c-axis patterns. In: Hobbes, B.E., and Heard, H.C. (Eds.) Mineral and Rock Deformation: Laboratory Studies - the Paterson Volume. American Geophysical Union, Geophysical Monograph 36, 263-286.

Sengupta, S., Roy, A., 2012. Tectonic Amalgamation of Crustal Blocks along Gadag-Mandya Shear Zone in Dharwar Craton of Southern India. Journal Geological Society of India 80, 75-88.

Sheppard, S., Rassmussen, B., Jian-Wei Zi, Soma Shekar, V., Srinivasa Sharma, D., Ram Mohan, M., Bryan, K., Simam, A. W., McNaughton N. J., 2017. Sedimentation and magmatism in the Paleoproterozoic Cuddapah basin, India: Consequences of lithospheric extension. Gondwana Research. https//doi.org/10.1016/j.gr.2017.04.024.

Silva, P.F., Marques, F.O., Machek, M., Henry, B., Hirt, A.M., Roxerová, Z., Madureira, P., Vratislav, S., 2014. Evidence for non-coaxiality of ferromagnetic and paramagnetic fabrics, developed during magma flow and cooling in a thick mafic dyke. Tectonophysics 629, 155-164.

Simpson, C., Schimd, S.M., 1983. An evaluation of criteria to deduce the sense of movement in sheared rocks. Geological Society of America 94, 1281-1288.

Sinha, R.M., Shrivastava, V.K., Sarma, G.V.G., Parthasarathy, T.N.1995. Geological favourability for unconformity related uranium deposits in northern parts of the Cuddapah Basin: evidences from Lambapur uranium occurrence, Andhra Pradesh, India. Exp. Res. At. Miner. 8, 111–126.

Stipp, M. and Tullis, J., 2003. The recrystallized grain size piezometer for quartz. Geophysical Research Letters, 30(21).

Tullis, J., Yund, R. A., 1991. Diffusion creep in feldspar aggregates: experimental evidence. Journal of Structural Geology 13, 987-1000.

Twiss, R.J., 1977. Theory and applicability of a recrystallized grain size paleopiezometer. In Stress in the Earth, Birkhäuser Basel. 227-244.

Verma, M.B., Som, A., Latha, A., Umamaheswar, K. and Maithani, P.B., 2008. Geochemistry of host granitoids oh uranium deposit at Chitril area, Srisailamsubbasin, Nalgonda District, Andhra Pradesh, Memoir Geological Society of India 73, 37-54.

Verma, M.B., Maithani, P. B., Chaki, A. Nageshwar Rao, P. and Prakher Kumar., 2009. Srisailam sub-basin, an uranium province of unconformity-related deposits in Andhra Pradesh – case study of Chitrial uranium exploration, Nalgonda District. Current Science 96, 588-591.

Yaouancq and Macleod, 2000 Yaouancq, G., MacLeod, C. J., 2000. Petrofabric investigation of gabbros from the Oman ophiolite: comparison between AMS and rock fabric. Marine Geophysical Researches 21, 289-306.

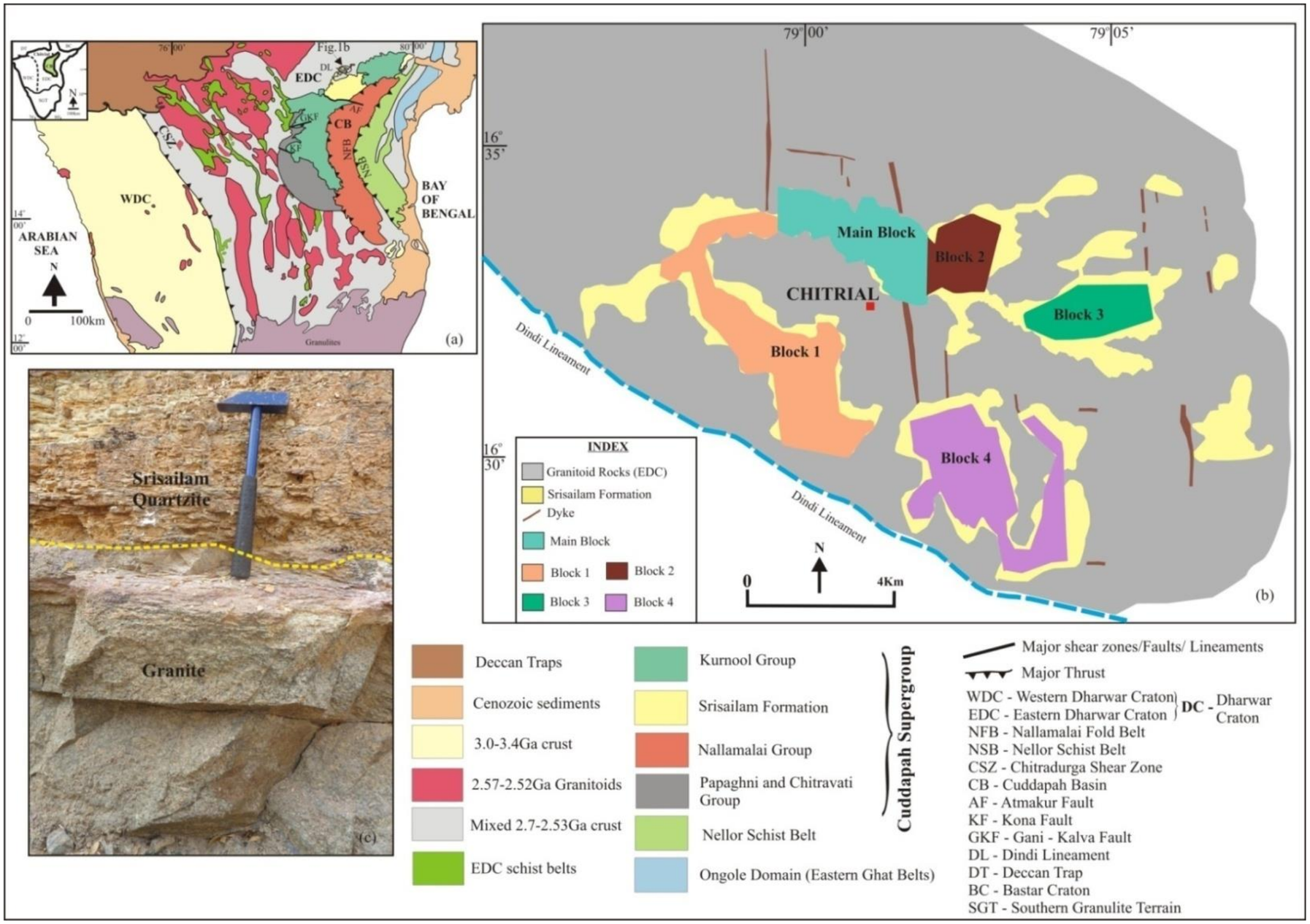

Fig. 1a The figure shows the geological map of south India depicting the Dharwar Craton, the Cuddapah Basin and the adjoining Nellore Schist Belt-Eastern Ghats Belt (Ongole Domain) (modified after Tripathy and Saha, 2013 and Jayananda et al., 2014). The ellipse denotes the present study area (Fig. 1b) where detailed work has been done. Inset: shows the different crustal blocks in the southern Indian shield. Fig. 1b Geological map of the study area around Chitrial (modified after Verma et al., 2008). The Chitrial outlier is sub divided into five blocks by AMD according to concentration of uranium mineralization. Fig. 1c Field photograph shows non conformity contact between basement granite and Srisailam quartzite.

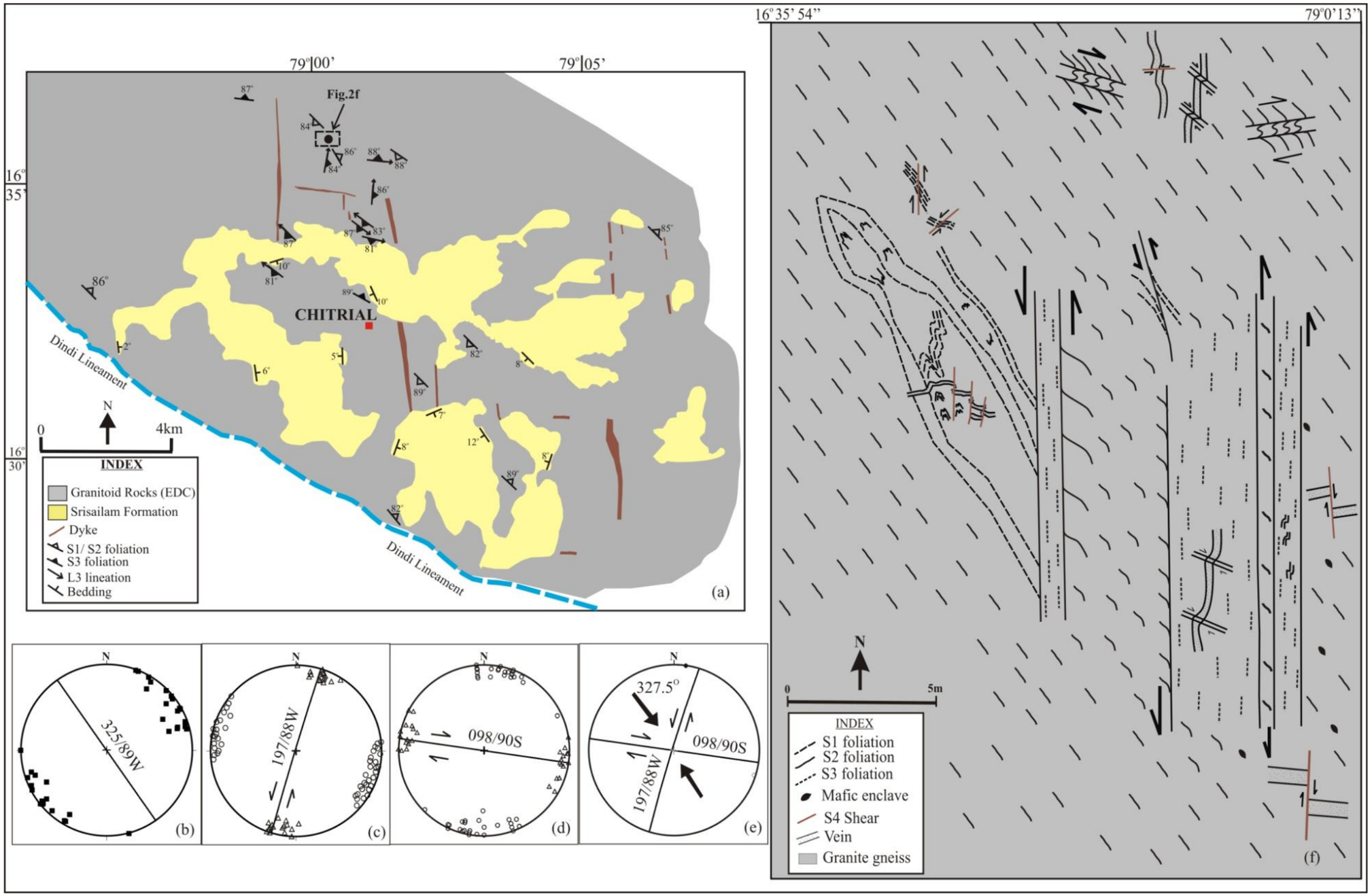

Fig. 2a Geological map of the study area around Chitrial (modified after Verma et al., 2008) showing the planar and linear structural elements of successive D1-D3 deformation phases. The blue trace in the map indicates the Dindi River. The dotted rectangle indicates the area where large-scale structural mapping (Fig. 2f) has been carried out; b-d) equal area plots of orientation data from granitoid, b) solid squares represent poles to S1-S2 planes, c-d) open circles represent poles to NNESSW and WNW-ESE trending S3 respectively and triangles represent related L3 lineation e) the girdles represent mean orientations of conjugate dszs, the black arrows indicate maximum compression direction (σ1; see text for detail). Fig.2f Large scale (1: 50 m) structural map prepared from a gneissic outcrop (see Fig. 2a for location) depicting the overprinting relationships among D1-D4 stage structural elements (see text for detailed description).

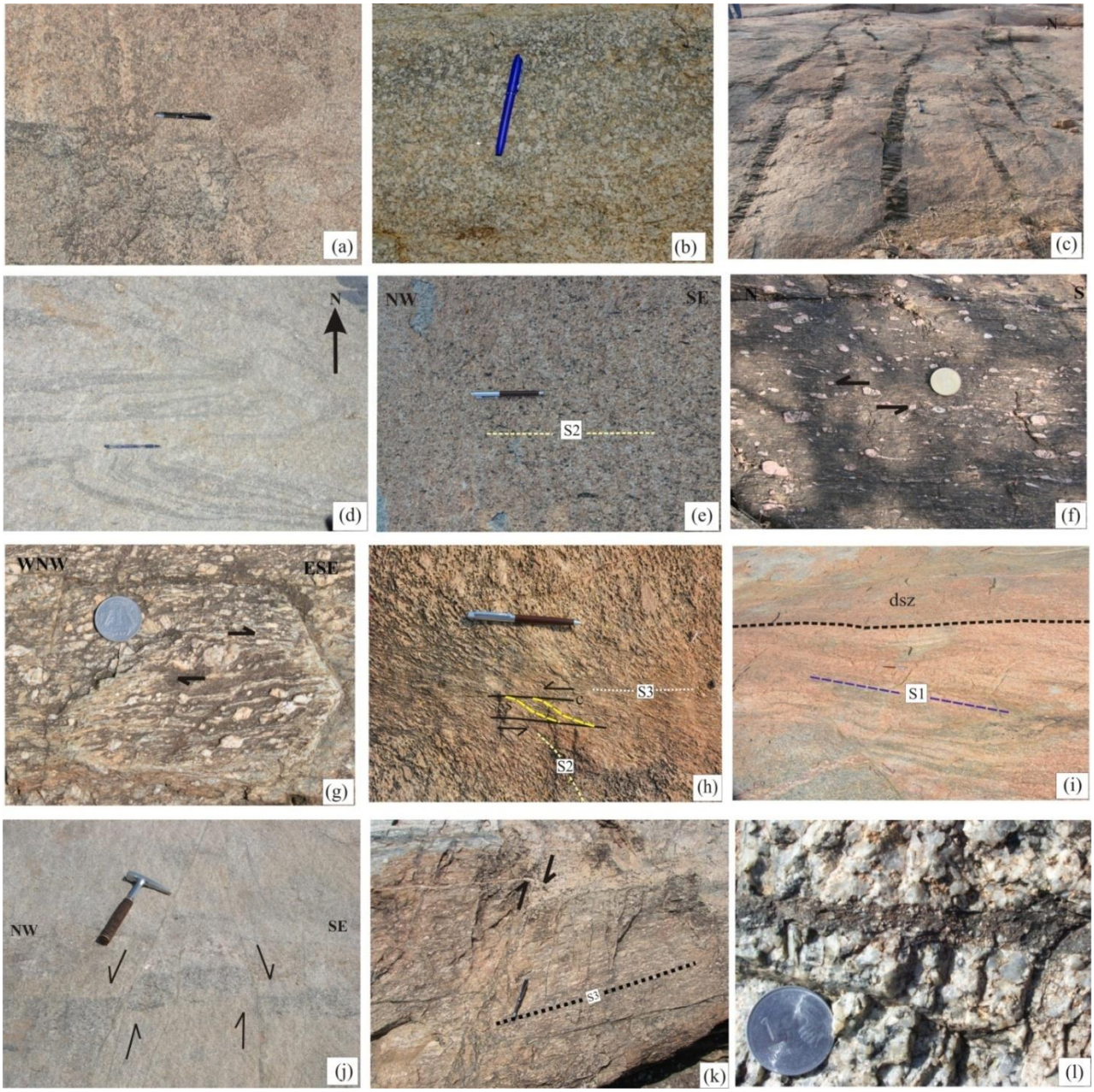

Fig. 3 Field photographs of a) massive granite b) porphyritic granite. c) basement granitoid cut by N-S trending dyke. d) NW-SE trending gneissic layering subjected to tight folding. e) NW-SE trending S2 foliation (yellow dotted line) defined by parallel biotite flakes. f-g) recrystallized asymmetric tails (σ structures) of feldspar porphyroclasts indicate sinistral and dextral shear sense along N-S and WNW-ESE shear zones respectively. h) N-S trending dsz develops transecting S2 planes at high angle in both walls, the S-C fabric developed within dsz indicates sinistral slip. i) development of outcrop scale dsz (black dashed lines indicate dsz boundaries) transecting S1 layering. j) development of conjugate shear planes displacing the S1 layering in basement granitoid. k) WNW trending mylonitic S3 fabric get dextrally displaced against a minor fault. l) narrow breccia zone developing within massive granite as a result of faulting.

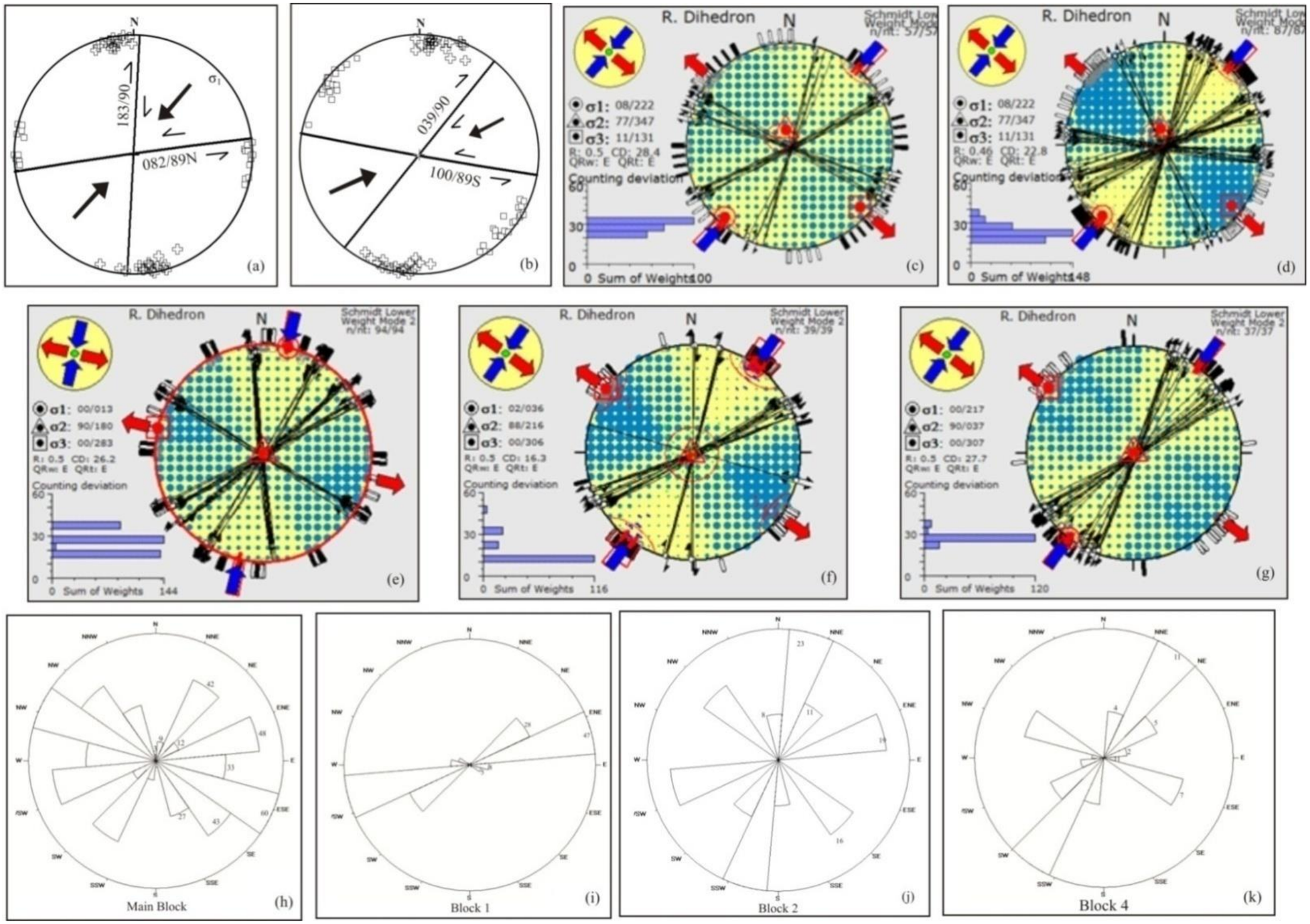

Fig. 4a-b) equal area plots of orientation data from D4 conjugate shear faults - open squares and crosses indicate poles to dextral and sinistral shear fault sets respectively, the girdles represent the mean orientations of the shear planes while the black arrows indicate maximum compression direction (σ1) deduced for each case (see text for detailed description). c-g) the orientation diagrams of conjugate shear planes occur in different subsets. Data analyzed by Win-Tensor program indicate the maximum principal stress directions from one representative site from each block. h-k) rose diagrams of one representative site from each block (main block, block 1, block 2 and block 4).

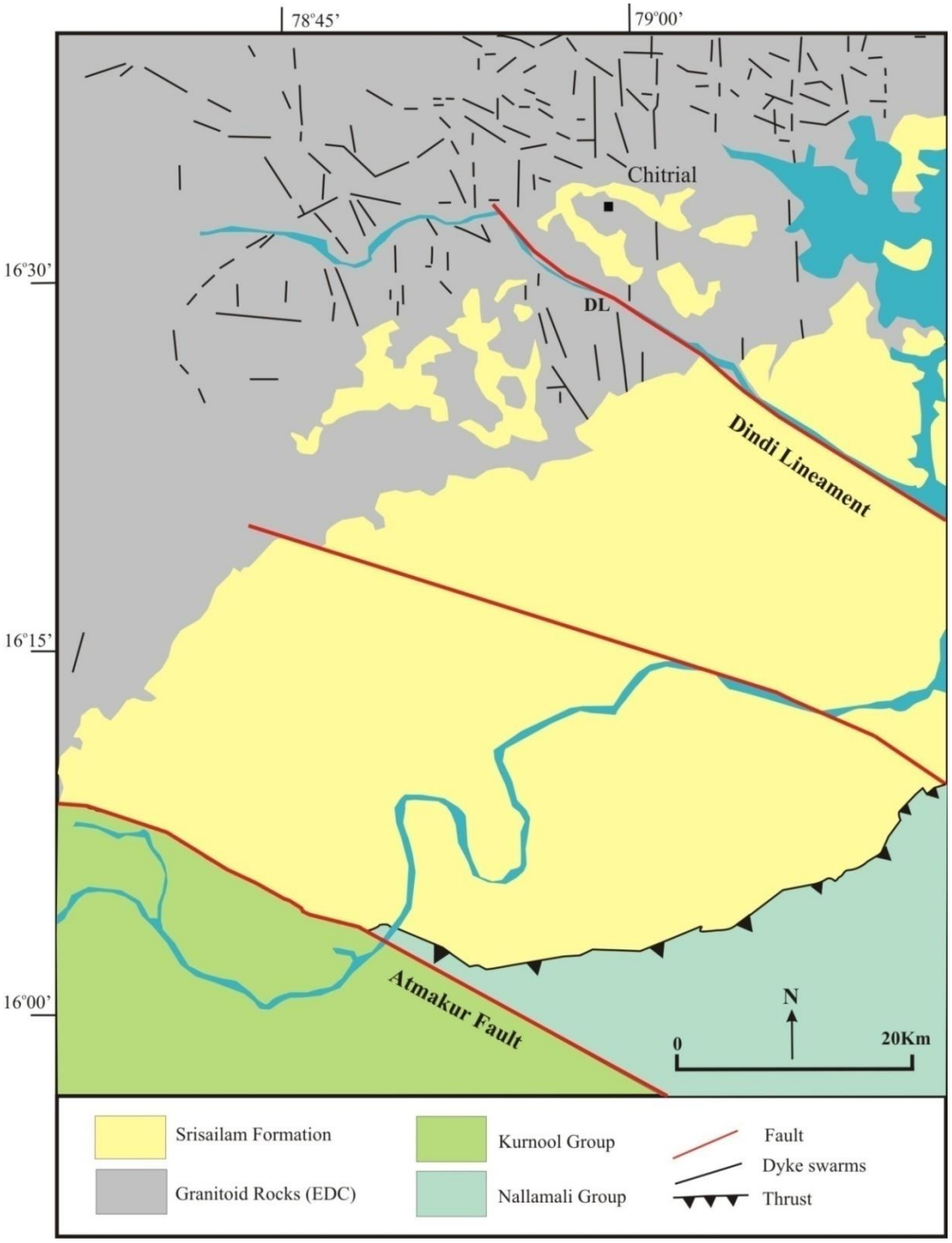

Fig.5 Geological map of the Srisailam sub-basin prepared from satellite imagery studies, showing the D5 stage large WNW-ESE trending faults, which displace the basement granitoid-Srisailam Formation contact.

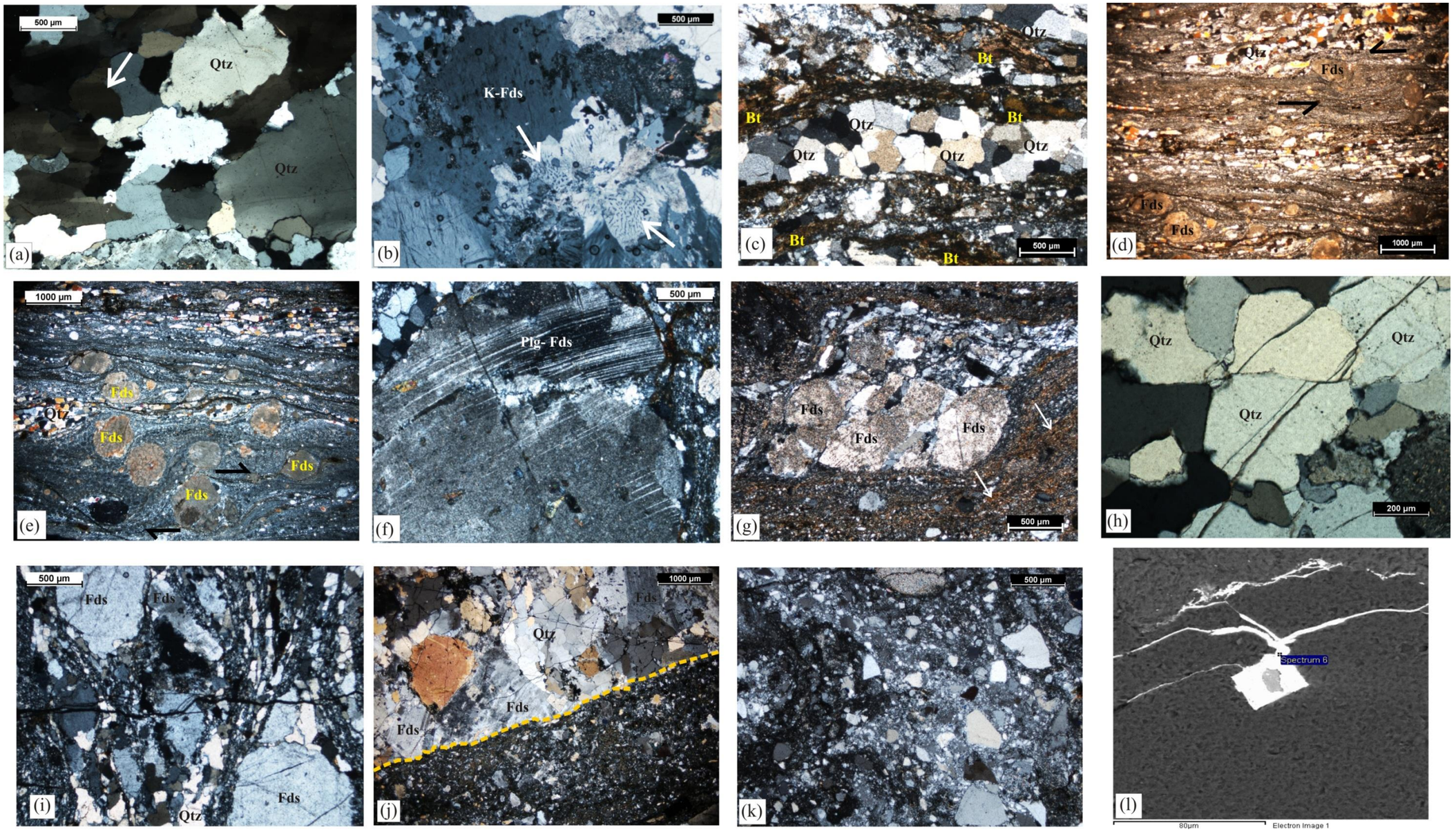

Fig.6 Photomicrographs showing D1-D4 stage microstructures from granitoids. a) interlocking texture composed of quartz (Qtz) and microcline (K-fds) within granite displaying magmatic texture. chessboard extinction pattern (marked by white arrow) in quartz indicating high –T solid state deformation. b) myrmekites developed along rims of K-feldspar grains. c) alternate quartz (Qtz)-plagioclase rich and biotite (Bt) rich layers defining S1 layering in granite gneiss. d-e) asymmetric recrystallized tails (σ-δ structures) of feldspar porphyroclasts in granite mylonites indicate sinistral and dextral shearing respectively. f) kinking and bending of deformation twins in Plagioclase feldspar (Plg-Fds).g) widespread recrystallization of feldspar clasts show grain tail complex and core-mantle structure. Biotite is marked by white arrow. h) transgranular fractures developing within the quartz grain (Qtz) massive granite. i) transgranular fractures cut across the S3 fabric. j) the cataclasite zones often show a sharp contact (yellow dashed line) with host rock. k) pulverized rock mass produced through cataclasis. l) Coffinite present along fracture.

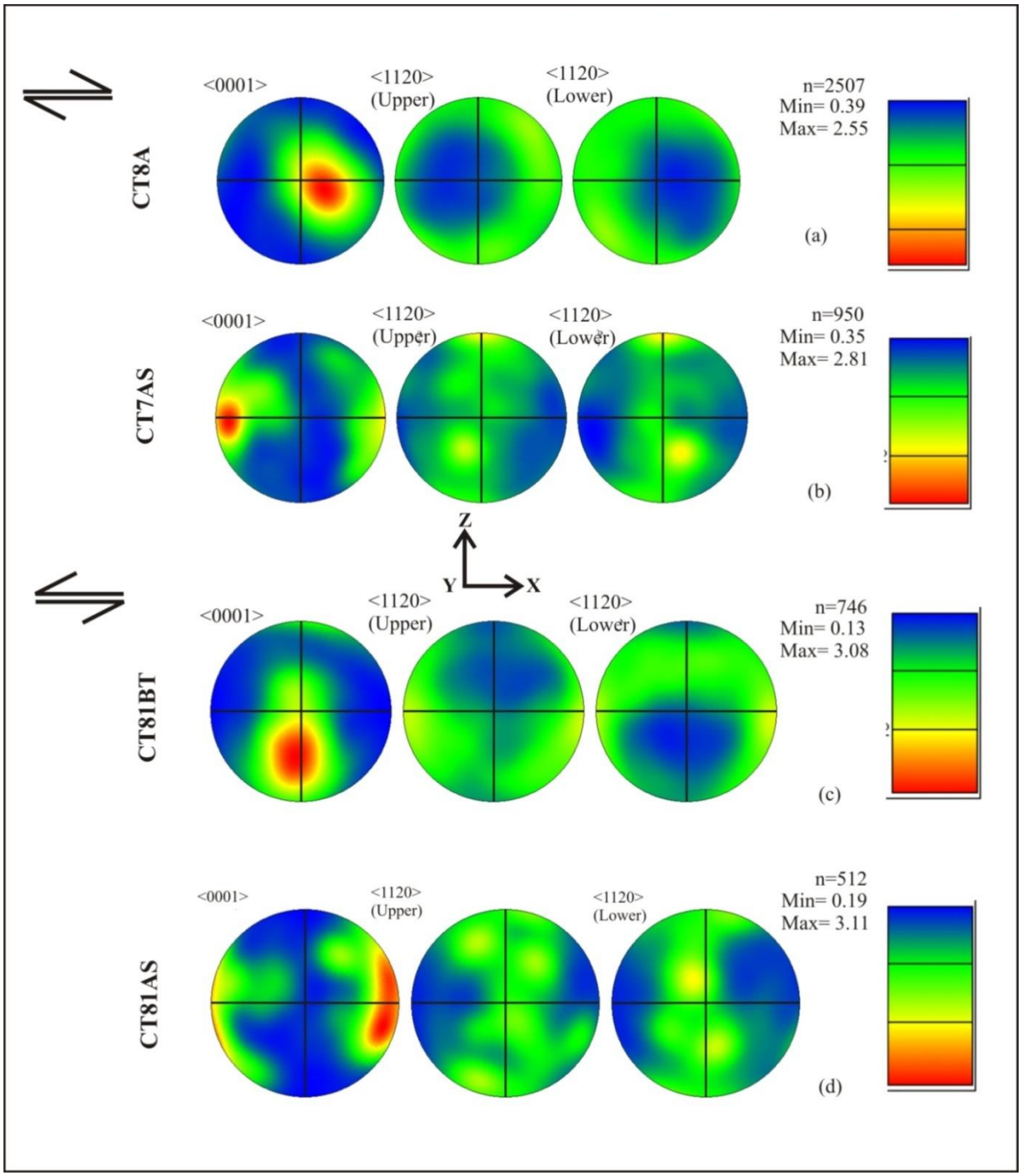

Fig. 7 Crystallographic orientation of recrystallized quartz grains, measured by EBSD method from four granite mylonite samples (see text for description of the samples), plotted in lower hemisphere equal area projections and contoured at interval uniform distribution. The number (n) of quartz analysis is shown. The arrows indicate sense of shear determined from inclination of single girdles with respect to foliation trace.

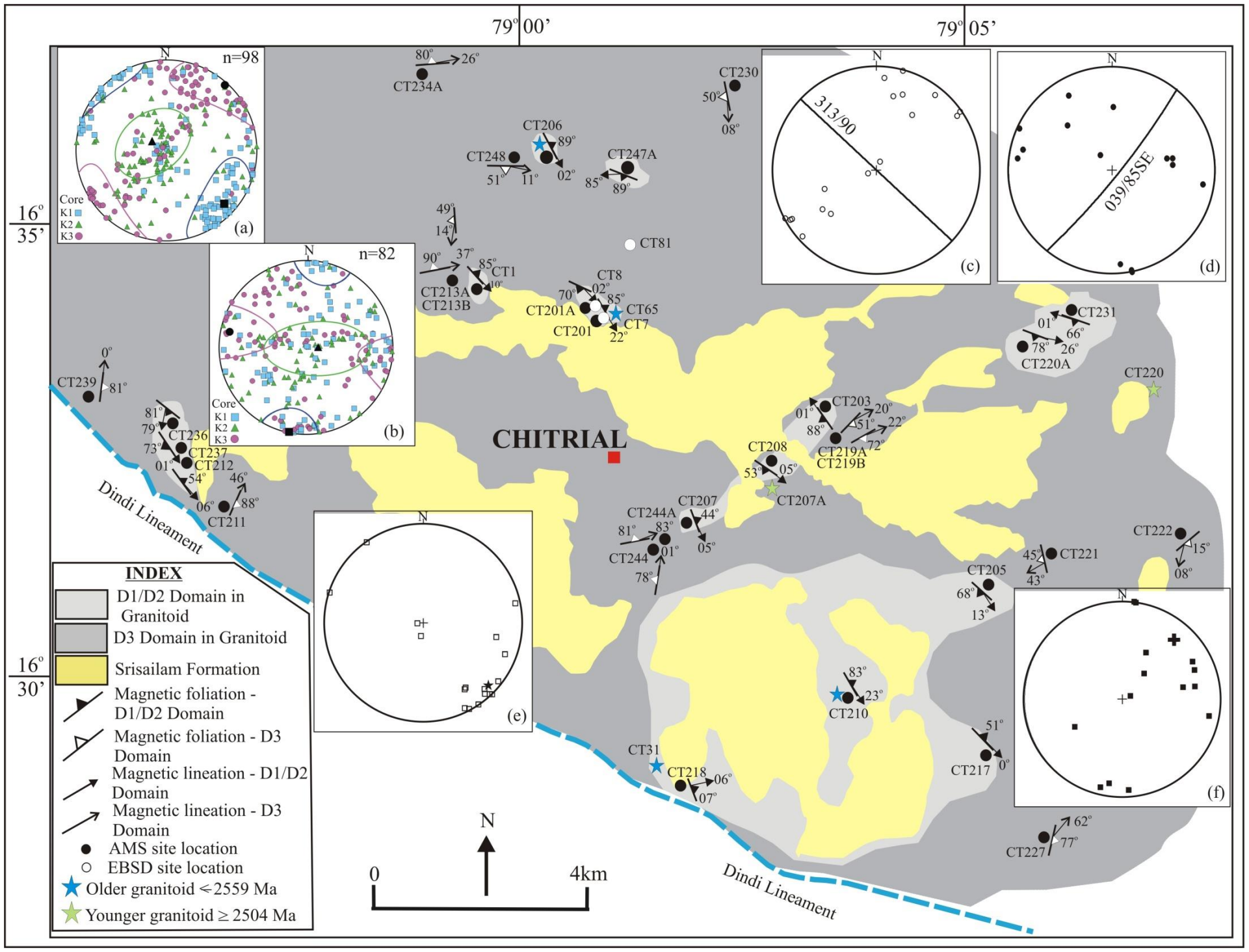

Fig. 8 Map showing sampling sites for AMS, EBSD and the geochronological age data as well as distribution of the D1-D2 and D3 domains (see text for detailed description). The blue trace in the map indicates the Dindi River. a)-b) Lower hemisphere equal area projections of AMS orientation data obtained using Anisoft 4. (AGICO, Czech Republic). Mean orientation (■ mean K1; ▲mean K2; ● mean K3) of the principle axes of the AMS ellipsoid, determine from the confidence ellipses. n=number of cores. c) -d) lower hemisphere equal area projection of mean K3 (pole to magnetic foliation) axes for 17 samples belonging to the NW'ly set and 14 samples belonging to the NE'ly set respectively. e) -f) lower hemisphere equal area projections of mean K1 axes (magnetic lineation) for 17 samples belonging to the NW'ly set and 14 samples belonging to the NE'ly set respectively. (For interpretation of the references to colour in this figure legend, the reader is referred to the Web version of this article.)

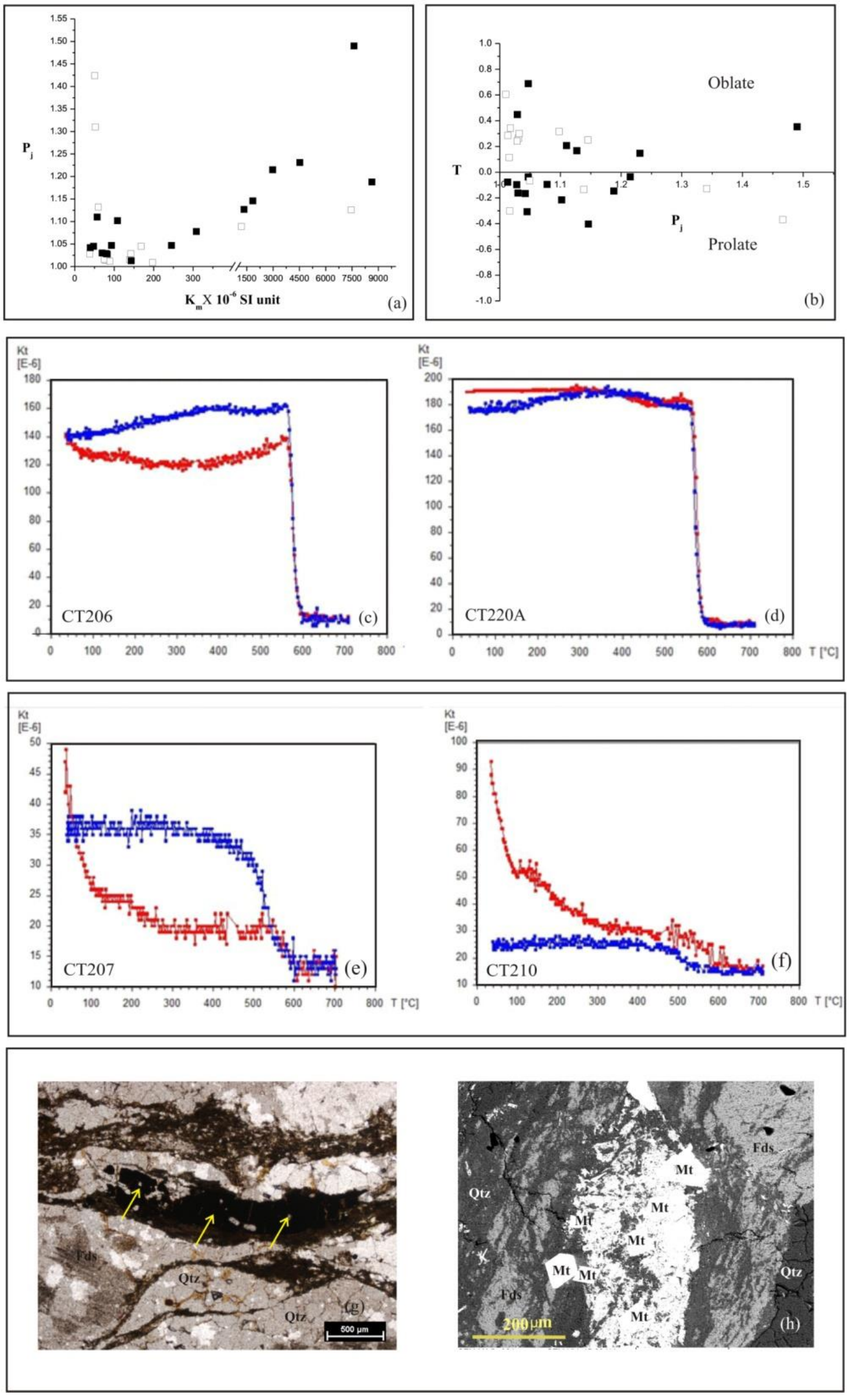

Fig. 9a-b) represent Km vs. Pj (Jelínek) and Pj vs. T (Jelínek) plots respectively for all the 31 analyzed granitoid samples analyzed in this study. The solid box represent the granitoid samples having dominant NW'ly of early D1/D2 domain as well as the open box represent the granitoid samples having dominant NE'ly magnetic fabric of later D3 domain. c-f) Temperature variation-magnetic susceptibility (k-T) plots. Note the sharp drop in susceptibility at 580 °C (Curie temperature of magnetite) of CT 206, and CT 220A while there is no significant drop at 580 °C for CT 207 and CT 210 samples. g) photomicrograph showing biotite (Bt) -magnetite (Mt) assemblage aligned parallel to the foliation traces defined by ribbon quartz (Qtz) and stretched feldspar (Fds). Yellow arrow indicates opaque minerals. h) BSE images of foliated granite showing magnetite (Mt) grains aligned parallel to foliation traces. (For interpretation of the references to colour in this figure legend, the reader is referred to the Web version of this article.)

	D1	D2	D3	D4	D5
Macro structures	—	—	—	—	Faults
Mesoscopic structures	Gneissic banding	Isoclinal folding of S1,	Conjugate sub-vertical shear zones (dsz)	Conjugate strike-slip faults	Faults & breccia
Microstructures	S1 Foliation	S2 Foliation	S3 mylonitic foliation	Solution seams, breccia &cataclasite	?
Kinematics	?	NE shortening	NNE sinistral& E-W dextral; NW shortening	N-NNE dextral & E-WNW sinistral; ENE to NE shortening	?
Magnetic Fabric	NW trending	NW trending	NE trending	—	—
Biotite	_____	_____	_____		
Magnetite		_____	_____		
Sericite				_____	
Chlorite				_____	
Timing		~2.55 Ga	~2.52 Ga	~1.8-1.6 Ga	≤ 0.5 Ga

Table. 1 Table shows characteristic features of the successive (D1-D5) deformation phases of the study area.

	SPO					
	R_{mf}	κ_{mf}	R_{qtz}	κ_{qtz}	R_{fds}	κ_{fds}
CT205	0.9	5.24	0.74	2.13	0.67	1.7
CT206	0.69	1.81	0.71	1.92	0.78	2.49
CT207	0.65	1.61	0.64	1.63	0.59	1.44
CT210	0.63	1.6	0.61	1.52	0.76	2.29
CT212	0.76	2.29	0.59	1.44	0.58	1.41
CT220A	0.68	1.75	0.72	1.99	0.65	1.61
CT236	0.69	1.81	0.67	1.7	0.68	1.75
CT221	0.67	1.7	0.68	1.75	0.54	1.28
CT227	0.75	2.21	0.69	1.81	0.75	2.21
CT230	0.6	1.5	0.71	1.92	0.71	1.92
CT234A	0.7	1.9	0.82	3	0.61	1.52
CT248	0.74	2.13	0.81	2.85	0.72	1.99

Table. 2 Shape preferred orientation (SPO) measurement data table for the analyzed 12 granitoid samples. SPO intensity parameters κ and R are determined separately for mafic (κ_{mf} and R_{mf}), quartz (κ_{qtz} and R_{qtz}) and feldspar (κ_{fds} and R_{fds}) grains (Piazolo and Passchier, 2002).

Sample no	Latitude	Longitude	Symmetry	Slip	Shear sense
CT8A	N16 33.878'	E78 59.870'	Monoclinic	prism <a>	Dextral
CT7AS	N16 33.850'	E78 59.88'	Monoclinic	prism <c>	Dextral
CT81BT	N16 34.638'	E79 0.363'	Orthorhombic	rhomb <a>	Sinistral
CT81AS	N16 34.638'	E79 0.363'	Monoclinic	prism <c>	Sinistral

Table. 3 Table shows details of the 4 granite mylonite samples (see Fig. 8 for sample locations), 2 each from sinistral slip and dextral slip dszs, from which EBSD data have been generated.

Sample no.	No. of grains	Average equivalent diameter (D)	Differential stress (Mpa)	
			Twiss (1977)	Stipp and Tullis (2003)
CT86E1	693	67.3	39	24
CT7AP	561	38.8	56	37
CT81AT	737	28.2	70	47
CT86E1	570	43.4	52	34
CT86AT	622	101.4	29	17
CT86F1	719	28.7	69	47
CT67BS	509	60.7	42	26
CT8A	400	123	26	15
CT8B	370	91.4	31	19
CT206	515	114.9	27	15
CT7AS	540	27.1	72	49
CT234a	521	32.3	64	42
CT248	525	29.7	68	45
CT81AS	605	18.1	95	68

Table. 4 Table shows calculation of Differential Stress using the experimentally derived piezometric equations of (Twiss, 1977) and (Stipp and Tullis, 2003) from the thin section (XZ section) of 14 mylonite sample.

.

Sample No.	Rock type	Lattitude	Longitude	No. of Specimen	K_m ($X10^{-6}$SI units)	P_j	T	L	K_1 D/I	K_2 D/I	K_3 D/I	Mean Magnetic Foliation (K_1K_2 Plane)
CT1	Granite gneiss	16°34'11.68"N	78°58'42.10"E	5	78.7	1.029	0.448	1.008	137/10	344/78	228/05	NW-SE/ vertical (313/90)
CT201	Granite gneiss	16°33'51.08"N	78°59'53.81"E	5	56.6	1.11	0.207	1.04	148/22	343/67	240/05	
CT201A	Massive granite	16°33'52.85"N	78°59'51.97"E	5	81.5	1.028	-0.097	1.015	137/02	228/05	023/83	
CT203	Massive granite	16°32'55.43"N	79° 02'52.33"E	6	93	1.047	0.688	1.01	325/01	199/87	055/02	
CT205	Massive granite	16°30'51.90"N	79° 04'48.20"E	6	2970	1.215	-0.036	1.103	111/13	222/58	013/28	
CT206	Granite gneiss	16°35'54.28"N	79° 0'12.78"E	5	7610	1.49	0.353	1.145	152/02	352/87	242/1	
CT207	Massive granite	16°31'35.29"N	79° 01'15.24"E	6	245	1.047	-0.037	1.023	154/05	059/43	250/46	
CT208	Massive granite	16°32'19.00"N	79° 02'7.73"E	5	69.1	1.03	-0.162	1.018	128/05	225/51	033/37	
CT210	Massive granite	16°29'50.60"N	79° 03'5.54"E	5	143	1.013	-0.077	1.007	147/23	345/65	240/07	
CT212	Massive granite	16°32'22.16"N	78°55'0.05"E	6	1340	1.127	0.167	1.053	139/06	041/52	234/36	
CT217	Massive granite	16°28'52.46"N	79° 4'44.87"E	8	47.3	1.045	-0.307	1.028	136/0	045/50	226/39	
CT218	Massive granite	16°28'32.77"N	79° 01'3.58"E	5	39.2	1.042	-0.166	1.021	078/06	348/01	248/83	
CT220A	Massive granite	16°33'40.54"N	79° 05'20.54"E	6	8630	1.188	-0.146	1.102	101/26	252/60	005/12	
CT231	Massive granite	16º34'9.2"N	79º 05'54.3"E	6	1840	1.146	-0.403	1.097	288/01	194/65	019/24	
CT236	Massive granite	16º 32'36.7"N	78º 54'54.5"E	6	308	1.078	-0.095	1.036	191/79	307/04	038/09	
CT237	Massive granite	16º 32'24.5"N	78º 54'56.3"E	6	4520	1.231	0.147	1.095	146/01	245/82	056/07	
CT247A	Massive granite	16°35'37.56"N	79° 01'21.96"E	7	108	1.102	-0.215	1.06	267/85	105/04	015/01	

CT211	Massive granite	16°31'47.50"N	78°55'34.28"E	5	37.9	1.028	0.265	1.01	027/46	202/42	294/02	NE-SW/ Subvertical (039/85SE)
CT213A	Massive granite	16°34'23.05"N	78°58'24.35"E	6	83.1	1.026	0.242	1.009	189/14	294/44	085/41	
CT213B	Massive granite	16°34.5'24"N	78°58'28"E	6	197	1.009	0.605	1.002	079/37	260/52	169/00	
CT219A	Massive granite	16°32'34.37"N	79° 03'5.44"E	6	77.9	1.014	0.114	1.007	062/20	173/43	315/39	
CT219B	Massive granite	16°30'34"N	79° 03'09"E	5	74.7	1.016	0.343	1.006	068/22	204/60	330/18	
CT221	Massive granite	16°31'13.94"N	79° 05'35.12"E	7	139	1.015	-0.301	1.01	240/43	338/09	078/45	
CT222	Massive granite	16°31'19.70"N	79° 07'7.86"E	5	88.8	1.012	0.286	1.003	194/08	103/11	322/75	
CT227	Massive granite	16°27'57.02"N	79° 05'24.18"E	6	1190	1.089	0.316	1.029	040/62	187/23	283/13	
CTS230	Massive granite	16º 36'50.6"N	79º 02'16.7"E	6	168	1.045	-0.065	1.023	176/08	275/48	079/40	
CT234A	Massive granite	16°37'4.66"N	78°58'4.37"E	6	142	1.029	0.301	1.009	080/26	284/61	175/10	
CT239	Massive granite	16º 33'3.8"N	78º 53'48.5"E	6	51.7	1.31	-0.128	1.161	007/00	097/80	277/09	
CT244	Massive granite	16º 31'19.6"N	79º 00'50.5"E	6	50.2	1.424	-0.368	1.261	008/01	270/77	099/12	
CT244A	Massive granite	16º 31'20.1"N	79º 00'58.7"E	6	59.5	1.132	0.252	1.048	069/83	259/06	169/01	
CT248	Massive granite	16°35'47.33"N	78°59'56.36"E	6	7450	1.126	-0.134	1.067	101/11	205/48	001/39	

Table. 5 AMS data for 31 analyzed granitoid samples of the study area. K_m = Mean susceptibility; P_j = corrected degree of magnetic anisotropy; T = shape of AMS ellipsoid (+ve = oblate & -ve = prolate); L = strength of magnetic lineation; K_1 and K_3 are Declination/Inclination of the Maximum and Minimum principal axes respectively of the AMS ellipsoid; n = number of cores per sample; Note: K_1 is the orientation of the magnetic lineation and K_3 is pole to the magnetic foliation (K_1K_2) plane, data for each location is the mean value obtained from analysis of multiple cores.